

1 A daily highest air temperature estimation method and
2 spatial-temporal changes analysis of high temperature in
3 China from 1979 to 2018

4 Ping Wang^{1,2*}, Kebiao Mao^{3*}, Fei Meng², Zhihao Qin³, Shu Fang⁴, Sayed M. Bateni⁵,
5 Mansour Almazroui^{6,7}

6 ¹ School of Physics and Electronic-Engineering, Ningxia University, Yinchuan 750021, China

7 ² School of Surveying and Geo-Informatics, Shandong Jianzhu University, Jinan 250100, China

8 ³ Institute of agricultural resources and regional planning, Chinese Academy of Agricultural
9 Sciences, Beijing 100081, China

10 ⁴ School of Earth Sciences and Resources, China University of Geosciences, Beijing 100083, China

11 ⁵ Department of Civil and Environmental Engineering and Water Resources Research Center,
12 University of Hawaii at Manoa, Honolulu, HI 96822, USA

13 ⁶ Centre of Excellence for Climate Change Research/Department of Meteorology, King Abdulaziz
14 University, Jeddah 21589, Saudi Arabia

15 ⁷ Climatic Research Unit, School of Environmental Sciences, University of East Anglia, Norwich,
16 UK

17 Correspondence to: Kebiao Mao (maokebiao@caas.cn)

18 ★ These authors contributed equally to this works.

19 **Abstract.** The daily highest air temperature (T_{\max}) is a key parameter for global and regional high
20 temperature analysis, which is very difficult to be obtained in areas where there are no
21 meteorological observation stations. This study proposes an estimation framework for obtaining
22 high-precision T_{\max} . Firstly, we build a near surface air temperature diurnal variation model to
23 estimate T_{\max} with a spatial resolution of 0.1° for China from 1979 to 2018 based on multi-source
24 data. Then in order to further improve the estimation accuracy, we divided China into six regions
25 according to climate conditions and topography, and established calibration models for different
26 regions. The analysis shows that the mean absolute error (MAE) of the dataset
27 (<https://doi.org/10.5281/zenodo.6322881>) after correction with the calibration models is about
28 1.07- °C, and the root mean square errors (RMSE) is about 1.52- °C, which improves the accuracy of
29 the traditional method by is higher than that before correction to nearly 1- °C. The spatial-temporal

30 variations analysis of T_{\max} in China indicated that the annual and seasonal mean T_{\max} in most areas
31 of China showed an increasing trend. In summer and autumn, the T_{\max} in northeast China increased
32 the fastest among the six regions, which were $0.4^{\circ}\text{C}/10\text{a}$ and $0.39^{\circ}\text{C}/10\text{a}$, respectively. The number
33 of summer days and warm days showed an increasing trend in all regions, while the number of icing
34 days and cold days showed a decreasing trend. The abnormal temperature changes mainly occurred
35 in El Niño years or La Niña years. We found that the influence of the Indian Ocean Basin Warming
36 (IOBW) on air temperature in China were generally greater than those of the North Atlantic
37 Oscillation and the NINO3.4 area sea surface temperature after making analysis of ocean climate
38 modal indices with air temperature. In general, this T_{\max} dataset and analysis are of great significance
39 to the study of climate change in China, especially for environmental protection.

40 **Keywords:** Near surface air temperature diurnal variation model; Daily highest air temperature; High temperature;
41 Spatial-temporal analysis; Climate change

42 **1 Introduction**

43 In the context of global warming, the frequency of high temperature events is increasing, and high
44 temperature tends to increase electricity demand and energy consumption (Zhang et al., 2021;
45 Sathaye et al., 2013), adversely affecting human health, social economy and ecosystem (Sehra et al.,
46 2020; Basu, 2009; Gasparrini and Armstrong, 2011). The daily highest air temperature (T_{\max}) is the
47 basic parameter for studying regional scale high-temperature events. It has a great influence on the
48 ozone concentration (Abdullah et al., 2017; Kleinert et al., 2021) and the start time of the plant
49 growth season on the Tibetan Plateau (Yang et al., 2017). T_{\max} is not only an important factor for
50 high temperature disaster risk assessment, but also a key input parameter for crop growth models
51 and carbon emission models. Sustained and abnormally high T_{\max} will cause high temperature heat

52 damage and adversely affect crop growth. Therefore, it is very important to accurately obtain the
53 temporal and spatial distribution of T_{\max} and study the characteristics of high temperature weather.
54 Generally, T_{\max} is measured on a thermometer in a louvered box 1.5 meters above the ground in the
55 field. Although the T_{\max} measured by this method has high accuracy but not spatial continuity.
56 Therefore, some scholars spatialized the station based T_{\max} through methods such as Kriging
57 interpolation and spline function interpolation. However, the number of meteorological stations is
58 limited, and stations in remote areas and areas with complex terrain are even sparser, which makes
59 the accuracy of T_{\max} obtained by interpolation difficult to meet the requirements of regional scale
60 research in China.

61 In order to obtain information about the spatial distribution of the T_{\max} , many scholars began to
62 use satellite remote sensing to solve this problem. There are three commonly remote sensing
63 methods to estimate T_{\max} . The first method is regression analysis, which uses the correlation
64 between retrieved land surface temperature (LST) and T_{\max} to establish a regression model to
65 estimate T_{\max} (Shen and Leptoukh, 2011; Evrendilek et al., 2012; Lin et al., 2012). The second
66 method is machine learning, which can flexibly estimate T_{\max} in urban areas with complex features
67 (Yoo et al., 2018). The third method is to use a diurnal temperature change model to extend the
68 instantaneous air temperature (T_a) to calculate T_{\max} , either by the Temperature-Vegetation Index
69 (TVX) method (Wloczyk et al., 2011; Zhu et al., 2013), the energy balance method (Sun et al., 2005;
70 Zhu et al., 2017), the atmospheric temperature profile extrapolation method (Fabiola and Mario,
71 2010), or other methods. The above methods of estimating T_{\max} with LST can better reflect the
72 spatial distribution of T_{\max} , but regression analysis and machine learning require sufficient and
73 representative samples, and the established model is not universal. TVX cannot estimate T_a at night

74 and in sparse vegetation areas. Many parameters required by the energy balance method cannot
75 usually be obtained by remote sensing technology. The estimation accuracy of atmospheric
76 temperature profile extrapolation method is greatly affected by the accuracy of the atmospheric
77 temperature profile. [The China Meteorological Administration \(CMA\) provided the grid dataset of](#)
78 [daily surface temperature in China \(V2.0\), which contains \$T_{\max}\$ data, but the spatial resolution of the](#)
79 [data is only \$0.5^\circ\$, and the data accuracy in local areas needs to be improved.](#) Therefore, a new method
80 for estimating T_{\max} needs to be proposed.

81 At present, most researches mainly used the extreme climate indices defined by the Expert Team
82 on Climate Change Detection and Indices (ETCCDI) to analyze the temporal and spatial distribution
83 characteristics of high temperature and its changing laws (Khan et al., 2018; McGree et al., 2019;
84 Poudel et al., 2020; Ruml et al., 2017; Salman et al., 2017; Wang et al., 2019; Zhang et al., 2019).
85 Zhou et al. (2016) analyzed the temperature indices changes in China from 1961 to 2010, and the
86 results indicated that the warm extremes in China exhibited an increasing trend. In addition, the
87 researchers analyzed the characteristics of high temperature changes in the Three River Headwaters,
88 Yangtze River Basin, Loess Plateau, Inner Mongolia and Songhua River Basin (Ding et al., 2018;
89 Guan et al., 2015; Sun et al., 2016; Tong et al., 2019; Zhong et al., 2017). In addition to analyzing
90 the temporal and spatial changes of high temperature events, many scholars have also studied the
91 influencing factors of high temperature events. Studies showed that extreme high temperature over
92 China was related to abnormal atmospheric circulation disturbances (You et al., 2011; Zhong et al.,
93 2017) and abnormal sea surface temperature (Li et al., 2019b; Wu et al., 2011). However, previous
94 studies on the cause of high temperature events usually only analyzed the correlation between

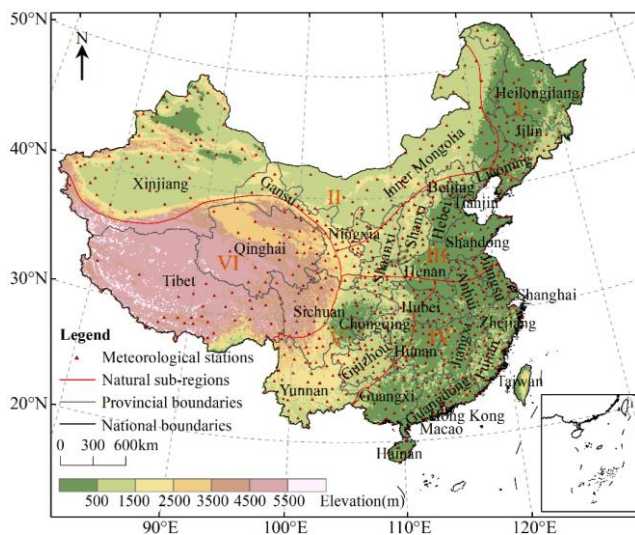
95 atmospheric circulation modes and the temperature indices along the time dimension, without
96 considering the spatial characteristics of the correlation.

97 From the above analysis, most of the researches mainly used the meteorological observation
98 temperature data interpolation to analyze local temperature changes, and as far as we know, no one
99 constructed continuous high-temporal resolution T_{\max} for high temperature analysis in China. In
100 order to better study regional high temperature events, this study proposes an estimation framework
101 for obtaining high-precision T_{\max} . Firstly, we used multi-source data and established near surface T_a
102 diurnal variation model to build T_{\max} dataset in China from 1979 to 2018 with a spatial resolution
103 of 0.1°. To further improve the accuracy, we divided China into six regions according to climate
104 conditions and topography, and established calibration models respectively. On this basis, we
105 further analyzed the spatial-temporal variation characteristics of T_{\max} and corresponding influencing
106 factors in China. This can provide evidence for mitigating global climate change and reducing
107 regional carbon emissions for environmental protection.

108 **2 Study area**

109 In order to establish a more high-precision T_{\max} dataset to analyze the temporal and spatial
110 characteristics of high-temperature in China, we divided China into six regions mainly based on
111 topographic conditions (elevation), and climatic conditions (T_a and precipitation), as shown in Fig. 1.
112 (I) The northeast region has a temperate monsoon climate. Affected by the monsoon, T_a in the
113 southern part of the region is higher than that in the north in winter. The topography of this area is
114 dominated by plains, hills, and mountains. Due to the influence of topography, the variability of T_a
115 is large in local areas. (II) The northwestern region is dominated by a temperate continental climate
116 (cold in winter and hot in summer) with a large annual and daily T_a range. The area exhibits little

117 annual precipitation which decreases from east to west. The topography of this area is dominated
 118 by plateau basins and rivers are scarce. (III) North China is located in a semi-humid and humid zone
 119 in the warm temperate zone. Precipitation is mainly concentrated in summer. This area is dominated
 120 by plains and plateaus, bounded by Taihang Mountain, the Loess Plateau in the west, and the North
 121 China Plain in the east. (IV) The southeast region is dominated by mountains and hills, which
 122 belongs to the warm and humid subtropical oceanic monsoon climate zone, and the tropical
 123 monsoon climate zone. The climate is mild, with an annual average T_a of 17-21 °C and an average
 124 rainfall of 1400-2000mm. (V) The southwestern region has a subtropical monsoon climate, affected
 125 by the southeast monsoon and southwest monsoon. It is hot and rainy in summers, and the landforms
 126 in this area are dominated by plateaus and mountains. (VI) The Qinghai-Tibet Plateau is located in
 127 southwest China, with an average elevation of more than 4,000 meters. The towering terrain has a
 128 great impact on the climate in eastern and southwestern China. It has a plateau mountainous climate,
 129 with cold winters and warm summers, with aridity and little rain throughout the year.



130

131 **Figure 1.** Overview of the study area.

132 **3 Data**

133 3.1 China Meteorological Forcing Dataset (CMFD)

134 CMFD is developed by the Hydro-meteorological Research Group of the Institute of Tibetan Plateau
135 Research, Chinese Academy of Sciences. The dataset can be obtained from the National Qinghai-
136 Tibet Plateau Science Data Center (<https://data.tpsc.ac.cn/>). The near surface T_a data of CMFD has
137 a time resolution of 3h and a spatial resolution of 0.1° , and its accuracy in China is better than Global
138 Land Data Assimilation System (GLDAS) data (He et al., 2020). CMFD data used ANUSPLIN
139 software to interpolate the difference between GLDAS T_a data and the measured T_a data to obtain
140 grid data, and then the difference grid data and the spatially downscaled GLDAS T_a data were
141 spatially added to generate high resolution T_a data. The T_a data of CMFD have been widely used in
142 climate simulation, hydrological simulation, vegetation greenness research, and cross-validation of
143 new T_a datasets (Luan et al., 2020; Gu et al., 2020; Wang et al., 2020). Although this dataset has
144 become one of the most widely used climate datasets in China, it does not provide the T_{max} value.
145 In order to perform high temperature analysis, we need to construct a T_{max} dataset.

146 3.2 ERA5 data

147 ERA5 data is the fifth generation of global climate reanalysis data produced by the European Centre
148 for Medium-range Weather Forecast (ECMWF) after ERA-Interim. The model version used by
149 ERA5 is IFS Cycle 41r2, and its spatial-temporal resolution and number of vertical layers are much
150 higher than the ERA-Interim data (Hoffmann et al., 2019; Urraca et al., 2018; Hersbach et al., 2020).
151 ERA5 reanalysis data provide a variety of meteorological elements, including atmospheric
152 parameters, land parameters, and ocean parameters, spanning a time range from 1950 to present.

153 The data can be obtained from Copernicus Climate Data Store (<https://cds.climate.copernicus.eu/>).
154 The ERA5 dataset also does not provide the T_{\max} . This study used T_a data from 1979 to 2018 with
155 a time resolution of 1 h and a spatial resolution of 0.25° to help build a T_{\max} estimation model to
156 generate T_{\max} value, and we ~~have performed multiple kinds of data assimilation~~ sampled the ERA5
157 data to the same spatial resolution as the CMFD data.

158 3.3 Meteorological station data

159 T_{\max} data from the China Surface Climatic Data Daily Dataset (V3.0) from 1979 to 2018 were used
160 to verify the accuracy of T_{\max} estimations. The hourly T_a observation data from China
161 meteorological stations were used to determine the occurrence times of T_{\max} and daily lowest air
162 temperature (T_{\min}). Both datasets are from CMA National Meteorological Information Center
163 (<http://data.cma.cn/>). The data were subjected to preliminary quality control and evaluation by CMA,
164 and all elements in the observational data are of high quality and completeness, with the validity
165 rate generally above 99%. These datasets have been widely used in Chinese climate research (Li et
166 al., 2019a; Tong et al., 2019). To ensure the validity of the site data, manual checks were performed
167 on all observed data, including extreme value tests and spatial-temporal consistency tests, and
168 continuous missing data due to instrument damage and other reasons were eliminated. There are
169 824 stations for T_{\max} observation data and 2633 stations for hourly T_a observation data. After
170 performing checks and tests, we used T_{\max} data from 760 meteorological ground stations and hourly
171 T_a data from 2421 meteorological ground stations.

172 3.4 Ocean climate modal indices

173 The ocean occupies about 71% of the earth's surface area, which has a great impact on climate
174 change. After considering the distribution characteristics of China's land and sea, we analyzed the

175 effects of the following ocean climate modal indices on high temperature in China: Indian Ocean
 176 Basin warming (IOBW) index, North Atlantic Oscillation (NAO) index, and NINO3.4 area sea
 177 surface temperature (NINO3.4) index. Among them, the IOBW index comes from the National
 178 Climate Center of CMA (<http://cmdp.ncc-cma.net/cn/index.htm>), and the NAO index and NINO3.4
 179 index are from the National Oceanic and Atmospheric Administration of the United States
 180 (<https://psl.noaa.gov/data/climateindices/list/>). The time range of the three indices is 1979-2018, and
 181 the time scale is monthly.

182 **Table 1. Overview of the data used in this study.**

	<u>China</u>	<u>China</u>	<u>China</u>	<u>Indian</u>	<u>Indian</u>	<u>Indian</u>	<u>NINO3.4</u>
<u>Data</u>	<u>Meteorological</u>	<u>ERA5</u>	<u>Surface Climatic</u>	<u>Hourly T_a observation data</u>	<u>Ocean Basin warming index</u>	<u>North Atlantic Oscillation index</u>	<u>area sea surface temperature index</u>
<u>Source</u>	<u>National Qinghai-Tibet Plateau Science Data Center</u>	<u>Copernicus Climate Data Store</u>	<u>CMA National Meteorological Information Center</u>	<u>CMA National Meteorological Information Center</u>	<u>National Climate Center of CMA</u>	<u>National Oceanic and Atmospheric Administration of the United States</u>	<u>National Oceanic and Atmospheric Administration of the United States</u>
<u>Description</u>	<u>T_a</u>	<u>T_a</u>	<u>T_{max}</u>	<u>T_a</u>	<u>=</u>	<u>=</u>	<u>=</u>
<u>Time span</u>	<u>1979-2018</u>	<u>1979-2018</u>	<u>1979-2018</u>	<u>1979-2018</u>	<u>1979-2018</u>	<u>1979-2018</u>	<u>1979-2018</u>

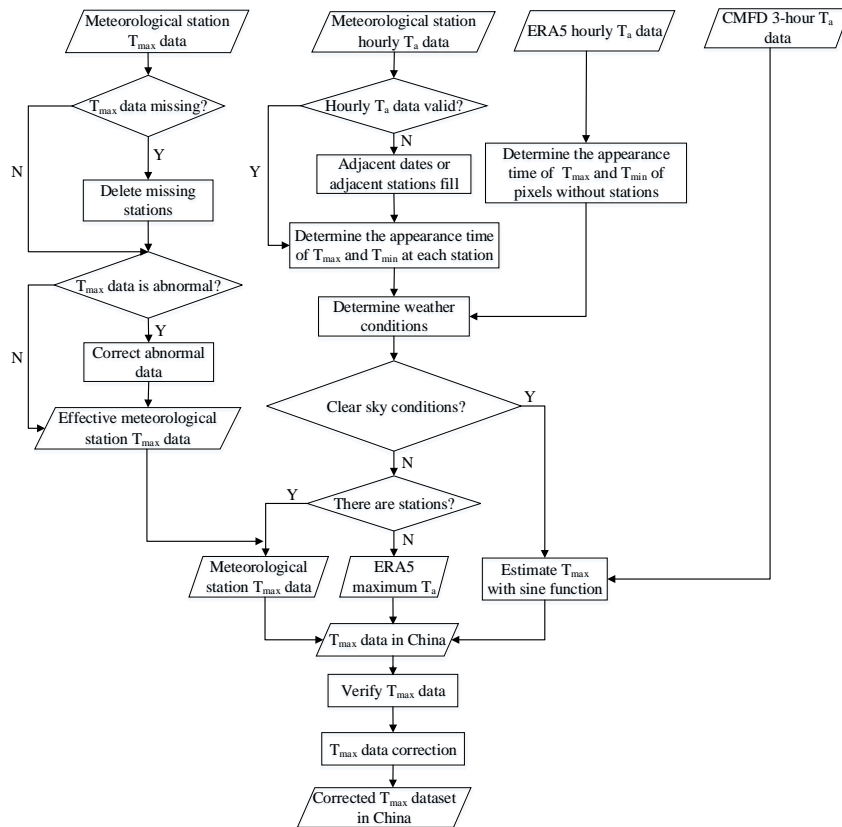
<u>Spatial/temporal resolution</u>	<u>0.1 °3 h</u>	<u>0.25 °1 h</u>	<u>-/1 d</u>	<u>-/1 h</u>	<u>-/1 month</u>	<u>-/1 month</u>	<u>-/1 month</u>
<u>Reference</u>	<u>(He et al., 2020)</u>	<u>(Hersbach et al., 2020)</u>	=	=	=	=	=
<u>Version</u>	=	=	<u>V3.0</u>	=	=	=	=
<u>DOI/URL</u>	<u>10.11888/AtmosphericPhysics.tpe.249369.file</u>	<u>10.24381/cds.adbb2d47</u>	=	=	=	=	=

4 Methodology

4.1 T_{\max} dataset construction

At present, the data used in the research on high temperature characteristics is mostly meteorological station data, or grid data obtained by interpolation of station data. A limited number of stations cannot represent the high temperature distribution at large scale. For regions where the stations are very sparse, grid data obtained by spatial interpolation can hardly meet the accuracy requirements of high temperature feature analysis. Although LST can be used to estimate T_{\max} , LST has degraded value in the presence of clouds or rainfall. Therefore, in order to obtain a T_{\max} dataset with high temporal and spatial resolution, we propose a T_{\max} construction model that combines meteorological station data and reanalysis data, and consider the T_{\max} construction under clear sky and non-clear sky conditions (see Section 4.1.1 for details). The data processing process is shown in Fig. 2, and the data construction model is divided into two steps: T_{\max} estimation and T_{\max} correction. First, the occurrence time of T_{\max} and T_{\min} was determined pixel by pixel (see Section 4.1.1 for details). Then, T_{\max} was determined according to the weather state. (1) In clear sky conditions, CMFD 3h near-surface T_a data was used to construct the T_a diurnal variation model which in turn yielded T_{\max} . (2)

198 In non-clear sky conditions, the site and reanalysis data were used to fill pixels. Finally, the
 199 correction model was used to correct the poor quality pixels to generate the final T_{\max} dataset in
 200 China.



201
 202 **Figure 2.** Technical roadmap for T_{\max} estimation.

203 4.1.1 T_{\max} estimation

204 The changes of T_a under different weather conditions are different. The changes of T_a under clear
 205 sky conditions are relatively smooth and regular. Under non-clear sky conditions, T_a changes more
 206 drastically. In order to improve the accuracy of T_{\max} estimation, we determined the occurrence time
 207 of T_{\max} and T_{\min} pixel by pixel. If there was a meteorological station at the pixel location, the analysis
 208 could be divided into two situations. (1) If hourly T_a data was valid, it was directly used to determine
 209 the occurrence time of T_{\max} and T_{\min} . (2) If there was a missing value in the hourly T_a data at a

210 certain time, then we used the valid data from adjacent stations at the same time or adjacent time at
 211 the same stations to fill in the missing values. At present, there are not many meteorological stations
 212 in China, and the pixels without stations account for 97.5%. If there was no meteorological station
 213 at the pixel location, we used ERA5 hourly T_a data to determine the occurrence time of T_{max} and
 214 T_{min} . Since the spatial resolution of the ERA5 data is lower than that of the dataset we produce, in
 215 order to match the two data spatially, we sample the two data to the same resolution, and then use
 216 latitude and longitude as control conditions to match the different data.

217 Studies have shown that the change of T_a under clear sky conditions follows a certain law: the
 218 change curve of T_a during the day is close to a sine function (Ephrath et al., 1996; Johnson and
 219 Fitzpatrick, 1977; Parton and Logan, 1981; Zhu et al., 2013), so we used sine function to simulate
 220 the change of T_a during the day. The appearance time of T_{min} is t_{min} , and the appearance time of
 221 T_{max} is t_{max} . According to the periodicity of the sine function, the model of the change of T_a during
 222 the day is obtained like Eq. (1).

$$223 \quad T_a(t) = A \sin\left(\frac{\pi(t-t_{min})}{t_{max}-t_{min}} - \frac{\pi}{2}\right) + B \quad (1)$$

$$224 \quad \begin{cases} \frac{\partial \delta}{\partial A} = \sum_{i=1}^n \left\{ 2 * \sin\left(\frac{\pi(t_i-t_{min})}{t_{max}-t_{min}} - \frac{\pi}{2}\right) * \left[A * \sin\left(\frac{\pi(t_i-t_{min})}{t_{max}-t_{min}} - \frac{\pi}{2}\right) + B - T_{ai} \right] \right\} = 0 \\ \frac{\partial \delta}{\partial B} = \sum_{i=1}^n \left\{ 2 * \left[A * \sin\left(\frac{\pi(t_i-t_{min})}{t_{max}-t_{min}} - \frac{\pi}{2}\right) + B - T_{ai} \right] \right\} = 0 \\ \delta = \sum_{i=1}^n \left[A * \sin\left(\frac{\pi(t_i-t_{min})}{t_{max}-t_{min}} - \frac{\pi}{2}\right) + B - T_{ai} \right]^2 \end{cases} \quad (2)$$

225 Here n is the number of CMFD near surface T_a data used to construct the T_a change model in a
 227 day. CMFD can obtain T_a data 8 times a day. This study uses four daytime T_a data to construct a T_a
 228 variation model, so n is 4. T_{ai} is the near surface T_a data at the i th time of CMFD, and δ is the sum
 229 of squares of the difference between the model estimated T_a and the near surface T_a of the CMFD.

230 Since the change of T_a under non-clear sky conditions does not conform to the sine curve change,
 231 we divided the estimation of T_{max} under non-clear sky conditions into two situations. (1) If there
 232 was a station at the location of the pixel, the measured T_{max} at the station was directly used as the
 233 T_{max} of the pixel. (2) If there was no measured T_{max} at the pixel location, the highest value of hourly
 234 T_a of ERA5 in a day was taken as T_{max} . Then T_{max} determined by the ERA5 data was assigned to
 235 the pixel at the corresponding position of the T_{max} image we established using the spatial matching
 236 method.

237 4.1.2 T_{\max} correction

238 The validation of T_{\max} showed some differences between the estimated T_{\max} and the measured T_{\max} .
239 In order to further improve the accuracy of T_{\max} , the measurements taken at weather stations should
240 be used to correct the estimated T_{\max} , as shown in Fig. 3. First, determine whether there is station
241 data at the pixel location. For pixels with stations, ~~it is further judged whether the difference~~
242 ~~between the estimated T_{\max} is valid by comparing and~~ the measured T_{\max} ~~with~~ less than 1 °C, we
243 ~~consider~~ the ~~estimated~~ T_{\max} ~~of this pixel to be valid~~. For a pixel with poor quality, if there is station
244 data at the location of the pixel, the low-quality pixel will be replaced with the measured data from
245 the station. If there is no station data at the pixel location, the data is corrected by ~~multiple~~-linear
246 regression method (Ninyerola et al., 2000; Zhao et al., 2020; Zheng et al., 2013). By establishing
247 the regression relationship ~~on each day~~ between station T_{\max} and estimated T_{\max} , the residuals were
248 calculated according to the measured values and T_{\max} regression predicted values, and the spatial
249 distribution of the residuals ~~on each day~~ was obtained by the inverse distance weight (IDW)
250 interpolation method. Finally, the estimated T_{\max} and the residual were added to obtain the corrected
251 T_{\max} . The calibration model is like Eq. (3) and Eq. (4).

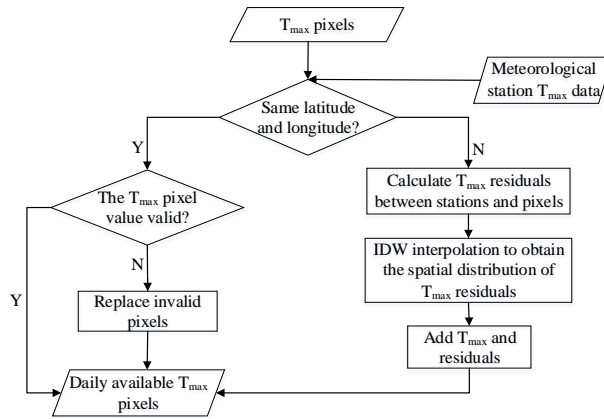
$$252 \quad T_{after}(i, j) = T_{before}(i, j) + \hat{\epsilon}(i, j) \quad (3)$$

$$253 \quad \hat{\epsilon}(i, j) = T_{true}(i, j) - T_{forecast}(i, j) \quad (4)$$

254 Here i and j are the row and column numbers of the image, $T_{after}(i, j)$ is T_{\max} after correction,
255 $T_{before}(i, j)$ is T_{\max} before correction, $\hat{\epsilon}(i, j)$ is the residual, $T_{true}(i, j)$ is the measured T_{\max} , and
256 $T_{forecast}(i, j)$ is T_{\max} predicted by the regression model.

257 We used the jackknife method to randomly divide the station data into calibration and
258 verification data (Benali et al., 2012; Zhao et al., 2020). We selected 80% of the meteorological
259 stations to establish the regression relationship between the measured and estimated T_{\max} values.
260 The other 20% of the meteorological stations were used to verify the accuracy of the corrected data.
261 In order to improve data accuracy, the dataset used in the subsequent analysis of spatial-temporal
262 variation of high temperature was the data corrected by all stations. Due to the different topographic
263 and climatic characteristics of the six natural regions, the linear models of estimated T_{\max} and

264 measured T_{max} in each region were different. In order to obtain a higher-precision correction, the six
 265 regions were corrected separately.



266
 267 **Figure 3.** Flow chart of T_{max} correction.

268 4.2 Extreme temperature indices

269 ETCCDI proposed a set of extreme climate indices in the Climate Change Monitoring conference,
 270 which became the unified standard for climate change research (Hong and Ying, 2018; Mcgree et
 271 al., 2019; Poudel et al., 2020; Zhang et al., 2019; Zhou et al., 2016). Among them, 27 indices are
 272 considered as core indices, which are calculated from daily T_a and precipitation data and have the
 273 characteristics of weak extremeness, low noise, and strong significance. These indices
 274 comprehensively capture the frequency, intensity and duration of extreme climate events, and are
 275 recommended as the core indicators for extreme climate event analysis by the STARDEX program
 276 of the European Union (Guan et al., 2015; Ruml et al., 2017). In this study, six temperature indices
 277 related to T_{max} were used to analyze high temperature characteristics, and their definitions are shown
 278 in Table 1. Among them, the 90th percentile in TX90p and the 10th percentile in TX10p were
 279 obtained in ascending order based on the T_{max} data of each month during 1979-2018.

280 **Table 12.** Definition of extreme temperature indices.

Index	Name	Definition	Category	Unit
-------	------	------------	----------	------

SU	Summer days	Annual count of days when $T_{\max} > 25^{\circ}\text{C}$	Frequency	d
TX90p	Warm days	Annual count of days when $T_{\max} > 90\text{th percentile}$	Frequency	d
TXn	Minimum T_{\max}	Annual minimum value of T_{\max}	Intensity	$^{\circ}\text{C}$
TXx	Maximum T_{\max}	Annual maximum value of T_{\max}	Intensity	$^{\circ}\text{C}$
ID	Icing days	Annual count of days when $T_{\max} < 0^{\circ}\text{C}$	Frequency	d
TX10p	Cold days	Annual count of days when $T_{\max} < 10\text{th percentile}$	Frequency	d

281 4.3 Trend analysis

282 4.3.1 Sen's slope estimation

283 In this study, the trends of T_{\max} and extreme temperature indices were calculated using Sen's slope
 284 estimation. Sen's slope estimation is a nonparametric estimation method. Even if there are some
 285 outliers in the sample, it can reliably estimate the change trend of the time series, so it is widely used
 286 in trend analysis (Sen, 1968; Zhang et al., 2017). The Eq. (5) is used to calculate the slope of each
 287 pair of data.

$$288 \quad K_i = \frac{x_k - x_j}{k - j} \quad (i = 1, 2, \dots, N) \quad (5)$$

289 Where $N = \frac{n(n-1)}{2}$, x_k and x_j are the time series values of the k th and j th samples respectively
 290 ($1 \leq j < k \leq n$). Arranging the N , K_i values in ascending order, the median Sen's slope is
 291 estimated as Eq. (6).

$$292 \quad \text{Slope} = \begin{cases} K_{[(N+1)/2]} & , N \text{ is odd} \\ \frac{K_{[N/2]} + K_{[(N+2)/2]}}{2} & , N \text{ is even} \end{cases} \quad (6)$$

293 4.3.2 Mann-Kendall trend test

294 Mann-Kendall trend test is used to test the trends of T_{\max} and extreme temperature indices. Mann-
 295 Kendall method does not require samples to follow a certain distribution and is not disturbed by a
 296 few outliers, and it can test the change trend of time series (Seenu and Jayakumar, 2021; Tan et al.,
 297 2019). Eq. (7) is used to calculate the statistic of the Mann-Kendall trend test.

$$298 \quad S = \sum_{i=1}^{n-1} \sum_{j=i+1}^n \text{sgn}(x_j - x_i) \quad (7)$$

$$299 \quad \text{sgn}(x_j - x_i) = \begin{cases} 1 & , x_j - x_i > 0 \\ 0 & , x_j - x_i = 0 \\ -1 & , x_j - x_i < 0 \end{cases} \quad (8)$$

$$300 \quad \text{Var}(S) = \frac{n(n-1)(2n+5)}{18} \quad (9)$$

301 Here x_i and x_j are the i th and j th data values of the time series, and n is the length of the time
 302 series, where n is 40. $\text{Var}(S)$ is the variance of S . The standardized statistic Z_c is computed by using
 303 Eq. (10).

$$304 \quad Z_c = \begin{cases} \frac{S-1}{\sqrt{\text{Var}(S)}}, S > 0 \\ 0, S = 0 \\ \frac{S+1}{\sqrt{\text{Var}(S)}}, S < 0 \end{cases} \quad (10)$$

305 When $|Z_c| > Z_{1-\alpha/2}$, the change trend is considered to be significant. Here, $Z_{1-\alpha/2}$ is the
 306 standard normal variance, α is the significance test level, when $\alpha = 0.05$, $Z_{1-\alpha/2} = 1.96$, and
 307 when $\alpha = 0.01$, $Z_{1-\alpha/2} = 2.58$.

308 4.4 Mann-Kendall test for abrupt change analysis

309 Climate system change is an unstable and discontinuous change process, and one of the commonly
 310 used methods to test its change is the Mann-Kendall mutation test, which is very effective in testing
 311 the change of elements from a relatively stable state to another state (Ruml et al., 2017). We used
 312 Mann-Kendall mutation test to test whether extreme temperature indices has mutation. For a time
 313 series x with n samples, Eq. (11) is used to construct an ordered sequence.

$$314 \quad s_k = \sum_{i=1}^k r_i \quad (k = 2, 3, \dots, n) \quad (11)$$

$$315 \quad r_i = \begin{cases} +1, x_i > x_j \\ 0, x_i \leq x_j \end{cases} \quad (j = 1, 2, \dots, i) \quad (12)$$

$$316 \quad UF_k = \frac{s_k - E(s_k)}{\sqrt{\text{Var}(s_k)}} \quad (k = 1, 2, \dots, n) \quad (13)$$

$$317 \quad E(s_k) = \frac{k(k-1)}{4} \quad (14)$$

$$318 \quad \text{Var}(s_k) = \frac{k(k-1)(2k+5)}{72} \quad (15)$$

319 Where s_k is the cumulative count of the number of values at time i greater than that at time j .
 320 $E(s_k)$ and $\text{Var}(s_k)$ are the mean and variance of the cumulative number s_k respectively. UF_k is a
 321 standard normal distribution, given the significance level α , and can be obtained from the normal
 322 distribution table. If $|UF_k| > U_\alpha$, which indicates that the variation trend of time series is significant.

323 Reverse the time series x to x_n, x_{n-1}, \dots, x_1 , and repeat the above process with $UB_k =$
324 $-UF_k (k = n, n - 1, \dots, 1)$.

325 4.5 Correlation analysis

326 Pearson correlation coefficient is often used to accurately measure the degree of correlation between
327 two variables, and its size can reflect the strength of the correlation of the variables. For
328 variables x_1, x_2, \dots, x_n and variables y_1, y_2, \dots, y_n , the correlation coefficient between them is
329 calculated as Eq. (16).

$$330 \quad R = \frac{n \sum_{i=1}^n (x_i y_i) - \sum_{i=1}^n x_i \sum_{i=1}^n y_i}{\sqrt{n \sum_{i=1}^n x_i^2 - (\sum_{i=1}^n x_i)^2} \sqrt{n \sum_{i=1}^n y_i^2 - (\sum_{i=1}^n y_i)^2}} \quad (16)$$

331 Here n is the total length of the time series. The value of R is between -1 and 1. $R < 0$ indicates a
332 negative correlation. $R > 0$ indicates a positive correlation. The closer the absolute value of R is to 1,
333 the closer the relationship between the two elements is.

334 5 Results

335 5.1 Validation

336 5.1.1 Validation of T_{\max} in each region

337 In order to verify the feasibility of T_{\max} estimation using the T_a diurnal variation model and to
338 analyze the accuracy of T_{\max} estimation in different regions, scatter plots of estimated T_{\max} and
339 measured T_{\max} in six natural regions (I, II, III, IV, V and VI) were drawn according to the regional
340 division in Fig. 1. The results are shown in Fig. 4, and the validation in each region shows that the
341 root mean square errors (RMSE) is between 2.38-2.94 °C, and the mean absolute error (MAE) is
342 between 1.88-2.45 °C, and the coefficient of determination (R^2) is between 0.95-0.99. In six regions,
343 the accuracy in region IV is the highest, while the accuracy is the lowest in region VI. As can be
344 seen from Fig. 4, although most of the data is very accurate, some have some room for improvement.
345 Therefore, further correction is needed to improve the accuracy of the T_{\max} dataset.

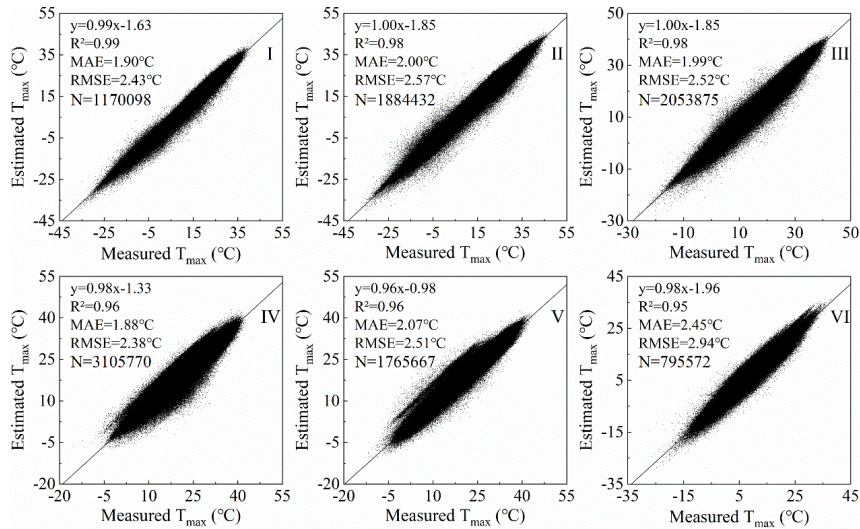


Figure 4. Validation of T_{max} estimation results in each region.

346

347

348

349

350

351

352

353

354

355

356

357

358

359

The correction method in Sect. 4.1.2 was used to correct the T_{max} estimation results of six regions separately. The comparison between T_{max} before and after correction with the measured T_{max} is shown in Fig. 5. It can be seen that T_{max} corrected by the regression model is more consistent with the measured T_{max} . The RMSE decreases from 2.38-2.94 °C to 1.14-1.81 °C, and the MAE decreases from 1.88-2.45 °C to 0.84-1.38 °C, and the R^2 increases from 0.96-0.99 to 0.97-0.99. The accuracy of T_{max} is improved in each region after correction. The number of meteorological stations in region I is denser, and the accuracy of T_{max} after calibration is significantly improved. The RMSE reduced from 2.32°C to 1.14°C, and the error is reduced by 51%. The number of meteorological stations in region VI is small, and the topography is undulating and the spatial heterogeneity is large. Therefore, the accuracy in this region is still the lowest among the six natural areas after correction. In general, the corrected T_{max} dataset has higher consistency with the measured data, and which can be applied to research related to regional scale T_{max} .

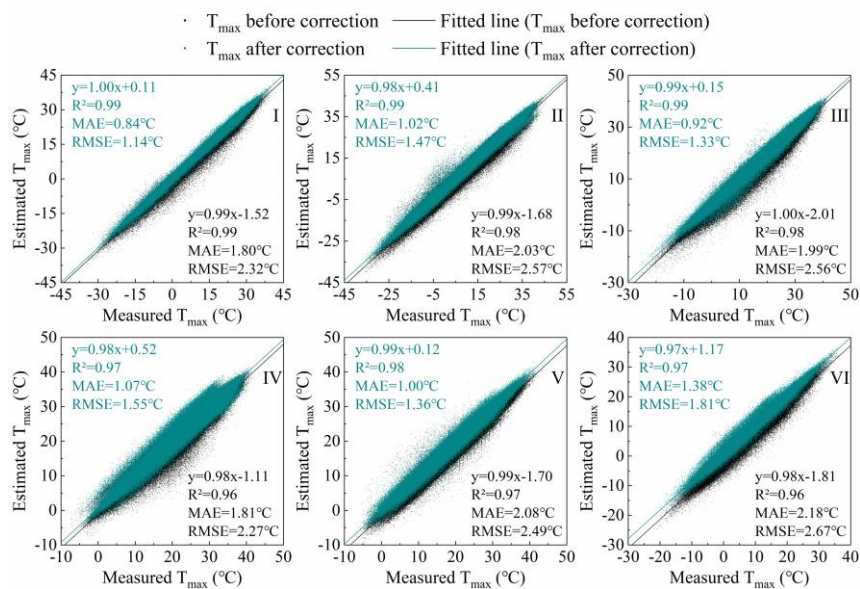
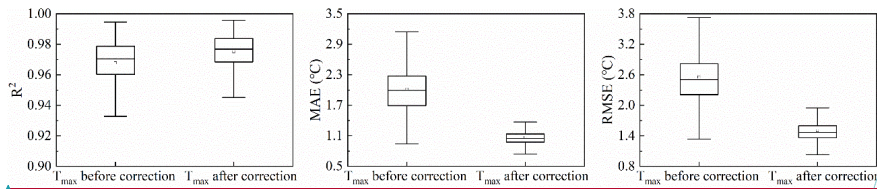


Figure 5. Validation of T_{\max} after correction.

5.1.2 Validation of T_{\max} in the whole China region

Figure 6 shows the accuracy of T_{\max} before correction and T_{\max} after correction for the entire China region. It can be seen that the MAE of the corrected dataset is about 1.07 °C, and the RMSE is 1.52 °C, which is nearly 1 °C higher than that before correction. The accuracy evaluation result of the dataset for different years shows that the dataset in 2008 has the highest accuracy and the lowest in 2014 (Fig. 7). It can be seen from Fig. 8 that the dataset has the highest accuracy in September and the lowest accuracy in December. This may be because there are more clear sky weather in China in September, and the daily temperature change curve is closer to a sine function, which makes the T_{\max} estimation result more accurate.

In general, the T_{\max} dataset has a time range of 1979-2018, in Celsius, with a temporal resolution of 1d and a spatial resolution of 0.1°. It is produced by using meteorological station data and T_a reanalysis data (CMFD and ERA5) combined with diurnal variation model of T_a to establish T_{\max} data, and then a correction model is constructed to further correct the data to improve the data accuracy according to different geographic partitions. The accuracy assessments indicate that the dataset exhibits high accuracy and can be used for climate change analysis in China.



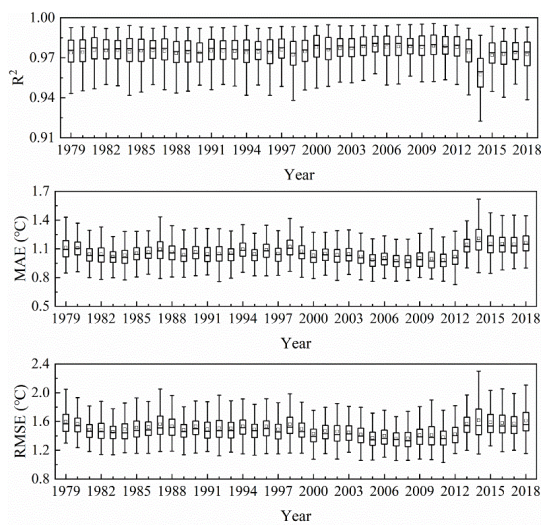
带格式的: 字体: (中文) 黑体, 五号

377

378

379

Figure 6. Box plots of the R^2 , MAE, and RMSE of comparison between T_{max} before correction and T_{max} after correction in the whole China region.

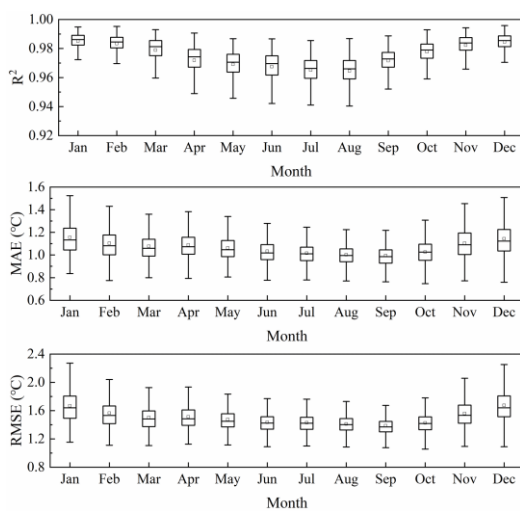


带格式的: 字体: (中文) 黑体, 五号

380

381

Figure 7. Box plots of the R^2 , MAE, and RMSE of T_{max} after correction for each year in the whole China region.



带格式的: 字体: (中文) 黑体, 五号

382

383 **Figure 8.** Box plots of the R^2 , MAE, and RMSE of T_{\max} after correction for each month in the whole China region.

384 5.2 Temporal and spatial changes of T_{\max}

385 5.2.1 Inter-annual variability

386 Fig. 69 shows the annual average change of T_{\max} in each region of China during 1979-2018. The
387 T_{\max} in each region exhibited an upward trend. However, due to the different geographical locations
388 and the influence of atmospheric circulation in various regions, the change of T_{\max} was also different.
389 The order of the T_{\max} increase in each region was: V>IV>III>Whole>VI>II>I. The T_{\max} anomaly
390 ranges of region I-VI and the whole China region were -1.41-1.53, -1.54-1.16, -1.47-1.12, -1.34-
391 0.92, -0.97-1.33, -1.31-1.15, and -1.09-0.98°C, respectively. The T_{\max} variation coefficients were
392 0.082, 0.045, 0.036, 0.024, 0.03, 0.088 and 0.038, respectively. It can be seen that T_{\max} fluctuated
393 the most in region VI and the least in region IV. The minimum values of region I-VI and China
394 region appeared in 1987, 1984, 1984, 1984, 1989, 1983, and 1984, respectively which were
395 distributed in the 1980s. The highest values of T_{\max} appeared in 2007, 2007, 2017, 2007, 2013, 1999,
396 and 2007 respectively. Zhai et al. (2016) found that 1999, 2007, and 2013 were among the 10 years
397 with the highest average T_a in China from 1900 to 2015. From 1998 to 2012, global surface
398 temperature experienced a warming hiatus (Du et al., 2019; Li et al., 2015), and T_{\max} in all regions
399 of China showed a downward trend during this period.

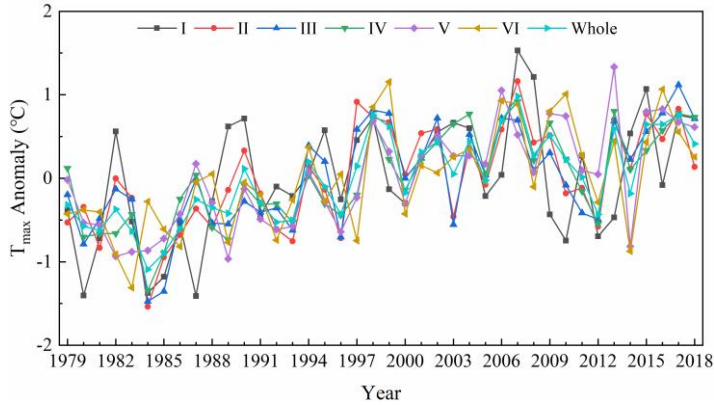


Figure 69. Inter-annual changes of T_{max} anomalies in six regions of China during 1979-2018.

In order to understand the spatial pattern and regional differences of T_{max} changes with more detail in China, Sen's slope estimation was used to calculate the annual average T_{max} change rate from 1979 to 2018 at the pixel scale (Fig. 7a10a). The significance test of the T_{max} change trend was conducted by the Mann-Kendall trend test (Fig. 7b10b). At the same time, the average change rate of T_{max} in each region and the area percentage of significant increase and decrease ($P < 0.05$) of T_{max} were calculated (Table 23). The results indicated that the annual average T_{max} change rate in most regions of China (78.24% of the study area) passed the significance test with a confidence significance level of 0.05, and 65.84% of the pixels showed very significant changes in T_{max} ($P < 0.01$). Fig. 7a10a showed that the annual average T_{max} in most regions of China was on the rise, and the fastest rising rate of T_{max} was in western Yunnan. Only 8.13% of the regions in China showed a downward trend in T_{max} . These were concentrated mainly in the north and south of Xinjiang, and the northwest and south of Tibet. Among the six regions, the average T_{max} change rate of region V was the largest ($0.38^{\circ}\text{C}/10\text{a}$), and the average T_{max} change rate of region I and region II was the lowest ($0.31^{\circ}\text{C}/10\text{a}$) (Table 23).

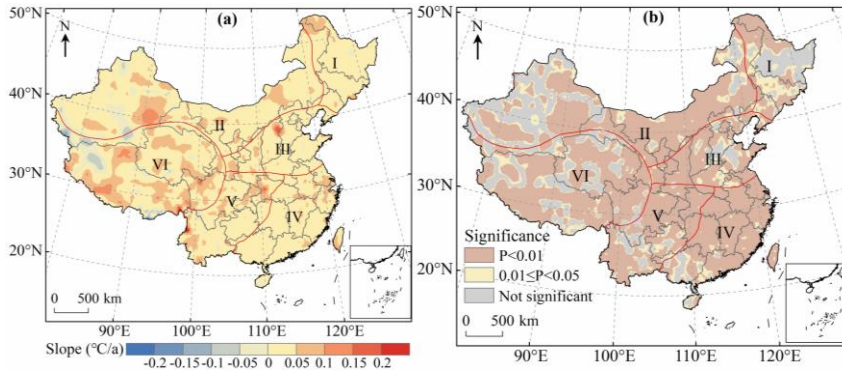


Figure 710. Inter-annual change rate of T_{\max} (a) and results of Mann-Kendall trend test (b).

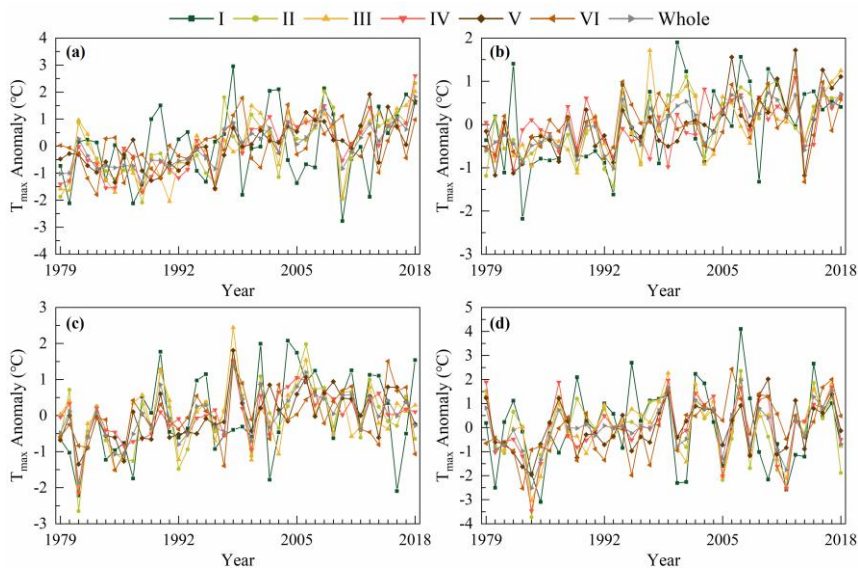
Table 23. Statistics of T_{\max} change trends in various regions of China from 1979 to 2018.

Region	I	II	III	IV	V	VI	Whole
Mean ($^{\circ}\text{C}/10\text{a}$)	0.31	0.31	0.33	0.35	0.38	0.33	0.33
Significant upward (%)	65.21	69.45	87.03	92.29	87.00	67.93	75.13
Significant downward (%)	0.09	3.14	0	0.32	0.75	7.92	3.11

419 5.2.2 Seasonal changes

420 On the basis of the annual analysis, we also analyzed the seasonal changes. The seasons are divided
 421 according to the months (spring from March to May, summer from June to August, autumn from
 422 September to November, and winter from December to February). We plotted the seasonal variation
 423 curve of T_{\max} in China from 1979 to 2018 (Fig. 811), and some information on the trend of T_{\max}
 424 changes is shown in Table 34. The results indicated that T_{\max} in each region fluctuated the most in
 425 winter and the least in summer. The highest T_{\max} in each region in spring, summer, autumn and
 426 winter mostly occurred in 2018, 2013, 1998 and 2007, while the minimum T_{\max} in each region in
 427 spring, summer, autumn and winter mostly occurred in 1988, 1993, 1981 and 1984. In 2013, T_{\max}
 428 of region IV-VI in summer reached the highest since 1979, mainly due to the influence of the
 429 southwest monsoon, East Asian summer monsoon and other factors. Under the influence of El Niño,

430 T_{\max} in winter in region I, II and the whole study area was the highest in 2007. Under the influence
 431 of La Niña, the minimum T_{\max} in spring and winter in most areas of China appeared in 1988 and
 432 1984, respectively. In the same season, the variation trend of T_{\max} in each region was significantly
 433 different, and some even had opposite trends. However, influenced by La Niña and the Eurasian
 434 atmospheric circulation, T_{\max} in winter in each region showed a consistent decreasing trend from
 435 2007 to 2008. As can be seen from Table 34, in spring, summer, autumn and winter, the regions
 436 with the fastest T_{\max} rise are III, I, I and VI respectively, and the regions with the lowest T_{\max} change
 437 rate are VI, VI, III and II respectively.



438
 439 **Figure 811.** Changes of T_{\max} anomalies in various regions of China in spring (a), summer (b), autumn (c), winter
 440 (d) during 1979-2018.

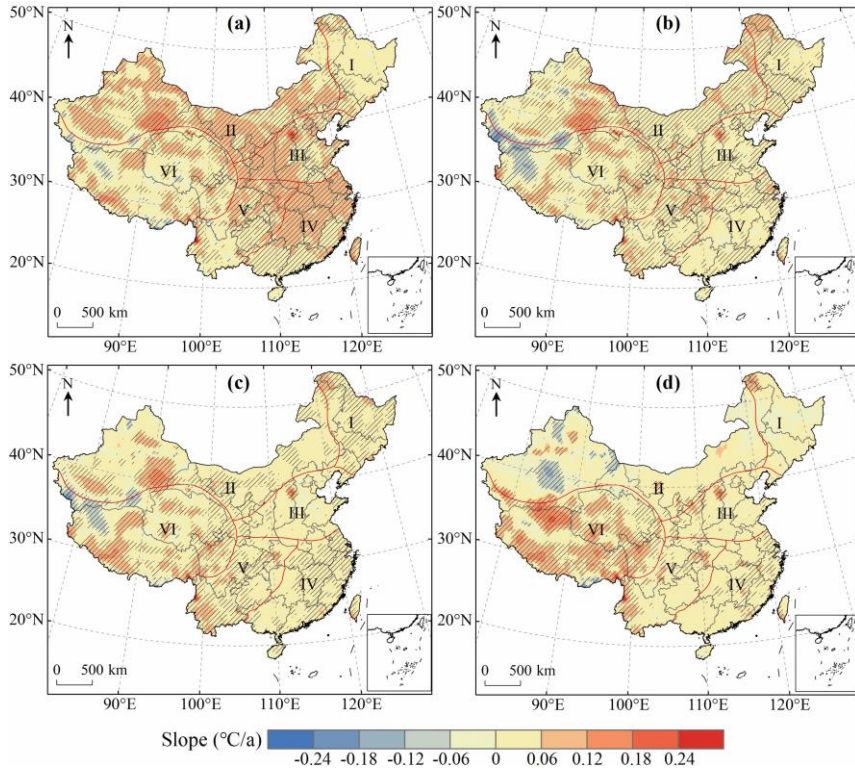
441 **Table 34.** Seasonal variation trend change rate of T_{\max} in various regions of China from 1979 to 2018.

	I	II	III	IV	V	VI	Whole
Spring	0.035	0.063**	0.072**	0.063**	0.051**	0.026*	0.048**
Summer	0.040**	0.035**	0.033**	0.022**	0.039**	0.020*	0.031**
Autumn	0.039*	0.024	0.014	0.025**	0.035**	0.025*	0.023**

Winter	0.009	-0.002	0.027	0.037	0.034*	0.058**	0.027
--------	-------	--------	-------	-------	--------	---------	-------

442 (*, ** represent the trends are significant at the level of $p=0.05$, $p=0.01$, respectively.)

443 In order to display the seasonal variation characteristics of T_{max} in China more intuitively, we
444 drew the spatial distribution of the trend of T_{max} and conducted a significance test (Fig. 9a12).
445 Meanwhile, we counted the percentage of significant increase and decrease of T_{max} in each region
446 (Table 45). The results indicated that the areas with increasing T_{max} were more than those with
447 decreasing T_{max} in all seasons. From 1979 to 2018, the increasing trend of T_{max} was most significant
448 in spring, which accounted for 92.73% of the total study area, followed by autumn and summer,
449 while T_{max} increased the least in winter. Specifically, T_{max} increased significantly in most parts of
450 China in spring, and the region where T_{max} decreased significantly were mainly concentrated in the
451 region VI (Fig. 9a12a). In summer, T_{max} in most part of China showed a significant increasing trend,
452 but T_{max} in southern Xinjiang and northwestern Tibet exhibited a decreasing trend (Fig. 9b12b).
453 Compared with spring and summer, the area with a significant increasing trend of T_{max} in autumn
454 was smaller, and the regions with a significant decreasing trend of T_{max} were mainly distributed in
455 Xinjiang and Tibet (Fig. 9c12c). 79.02% of the regions experienced an increase in T_{max} in winter,
456 which was significantly lower than in other seasons. A significant increasing trend of T_{max} was
457 observed in the east of region IV, the southwest of regions V and VI, while the areas where T_{max}
458 decreased significantly were mainly observed in Xinjiang (Fig. 9d12d). We also observed no
459 significant decrease in T_{max} in regions I and III in spring, I in summer, I and IV in autumn, and III
460 in winter (Table 45). Further statistics showed that T_{max} of the whole region III showed an upward
461 trend in spring.



462
463 **Figure 912.** Spatial distribution of the change trend of T_{\max} in spring (a), summer (b), autumn (c), winter (d) over
464 China during 1979-2018. The shaded areas indicate trends that are significant at the 0.05 level.

465 **Table 45.** Change trend statistics of T_{\max} in different seasons over China from 1979 to 2018.

	Significant upward (%)				Significant downward (%)			
	Spring	Summer	Autumn	Winter	Spring	Summer	Autumn	Winter
I	35.12	74.75	65.75	6.89	0	0	0	0.10
II	81.56	73.47	36.07	8.10	1.01	7.04	3.15	10.87
III	97.71	69.05	14.67	15.99	0	0.38	0.06	0
IV	96.20	46.80	57.26	29.47	0.35	0.68	0	0.44
V	76.48	75.11	58.56	31.62	1.24	1.53	0.06	0.12
VI	50.20	55.11	49.54	68.58	7.00	14.17	10.34	2.28
Whole	71.46	65.39	45.86	29.40	2.29	6.04	3.61	4.01

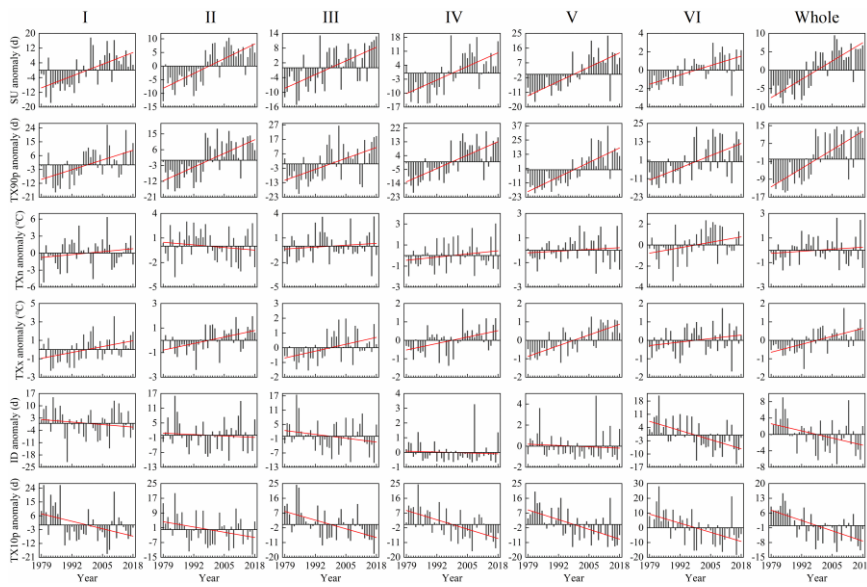
带格式的: 字体: 加粗

466 5.3 Temporal and spatial changes of extreme temperature indices

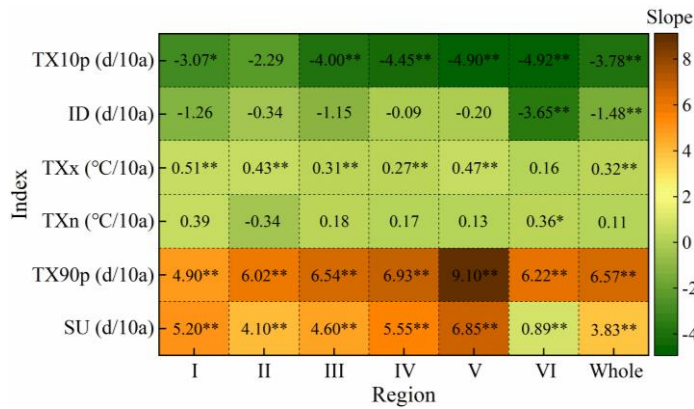
467 5.3.1 Change of time

468 We plotted the inter-annual variation of extreme temperature indices anomalies in various regions
469 of China from 1979 to 2018 (Fig. 4013), and used Sen's slope estimation and the Mann-Kendall
470 trend test to calculate statistics on the trend of extreme temperature indices (Fig. 4414). The results
471 indicated that SU, TX90p, TXn and TXx increased at a rate of 3.83d/10a, 6.57d/10a, 0.11°C/10a
472 and 0.32°C/10a, respectively (Fig. 4414). Influenced by the strong El Niño in 1997, the SU in all
473 regions exhibited a consistent upward trend from 1996 to 1997 (Fig. 4013). The change rate of SU
474 in all regions passed the significance test of 0.01, indicating a significant upward trend (Fig. 4414).
475 The increasing trend of TX90p in all regions was also very significant. The decadal average of
476 TX90p in region III-VI and the whole study area had an increasing trend, while the decadal average
477 of TX90p in region I and region II increased first and then decreased slightly. The TXn of region II
478 showed a weak decreasing trend, and the sliding average of the 3-year and 5-year periods also
479 exhibited a weak fluctuation downward trend. TXn of other regions showed an upward trend in
480 general, and only region VI had a significant increasing trend ($P < 0.05$) (Fig. 4414). Except for
481 region VI, the change rate of TXx in other regions was higher than that of TXn. The rate of change
482 of TXx exhibited that the upward trend of region VI was not significant, while all other regions
483 passed the significance test of 0.01. During 1979-2018, ID and TX10p decreased significantly at the
484 rate of -1.48d/10a and -3.78d /10a, respectively ($P < 0.01$) (Fig. 4414). The ID of all regions
485 exhibited a downward trend, with region VI and the whole study area showing the most obvious
486 decline, passing the significance test of 0.01 (Fig. 4414). Compared with ID, TX10p decreased more
487 sharply, and the highest value of TX10p in all regions occurred before 1988 (Fig. 4013). The above
488 results indicate that the frequency of high temperature events in China is on the rise, which is in line
489 with the expected results of global change. In addition, we also found that the occurrence time of

490 maximum and minimum values of SU, TXn, TXx and ID during 1979-2018 was consistent with
 491 previous research results by Hong and Ying (2018), which further proved the correctness of the T_{max}
 492 dataset constructed by us, indicating that the dataset can be used to analyze the spatial-temporal
 493 changes of high temperature in China.



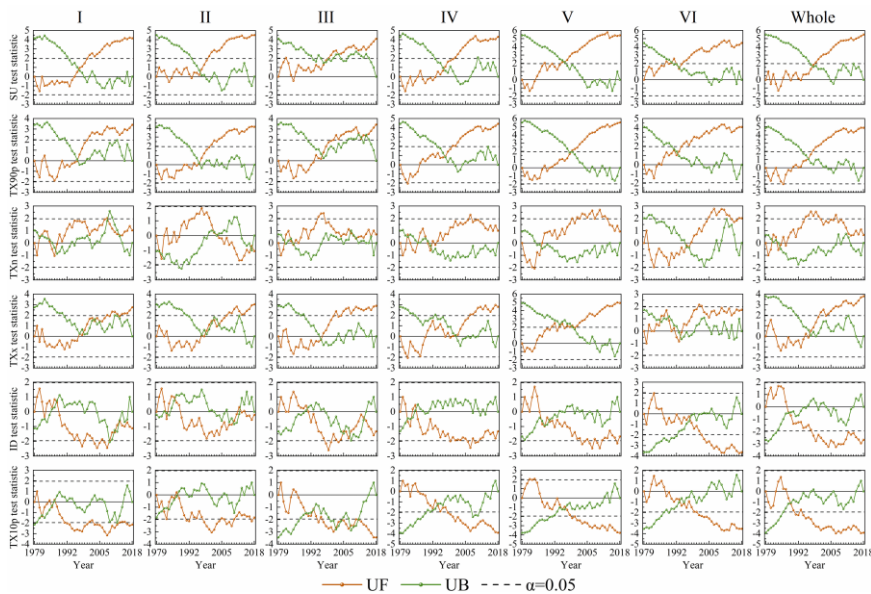
494
 495 **Figure 4013.** Inter-annual trend of extreme temperature indices anomalies in different regions of China during
 496 1979-2018.



497

498 **Figure 11.14.** Variation trend of extreme temperature indices in different regions of China from 1979 to 2018. (*
 499 significant at the 0.05 level, ** significant at the 0.01 level.)

500 In order to analyze the variation rules of extreme temperature indices in China from 1979 to
 501 2018, the Mann-Kendall mutation test was applied to test the mutation characteristics of six extreme
 502 temperature indices at the significance level of 0.05. The results are shown in Fig. 11.15. We found
 503 that all the extreme temperature indices had abrupt change from 1979 to 2018, and 40% of the years
 504 where the abrupt changes occurred were El Niño years, while 46.7% were La Niña years. This
 505 finding further confirms that China is greatly affected by global climate change. TX90p in region I-
 506 II and the whole study area displayed an abrupt change from a period with lower value to one with
 507 higher value in 1996. After mutation in region II in 2003, TXn turned from an upward trend to a
 508 downward trend, but the downward trend was not obvious. The ID of the whole study area and its
 509 six sub-regions tended to increase first and then decrease.



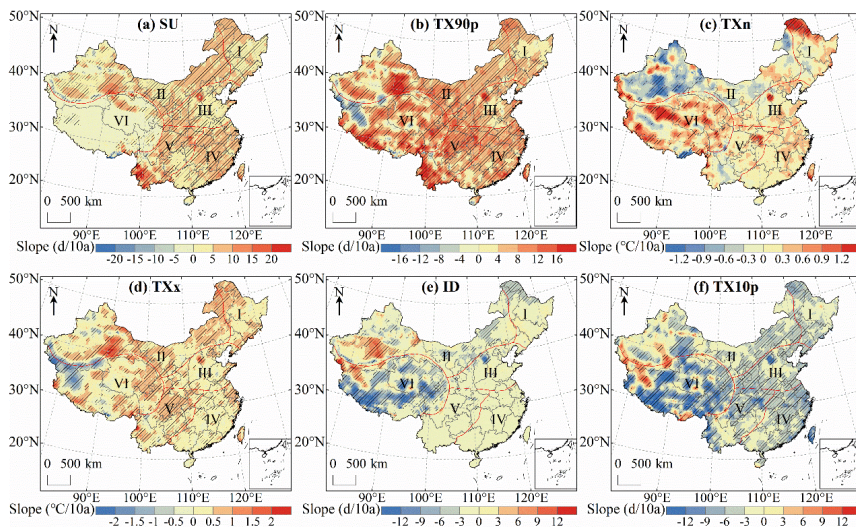
510

511 **Figure 4215.** MK abrupt change detection for the extreme temperature indices in different regions of China during
512 1979-2018.

513 5.3.2 Spatial change

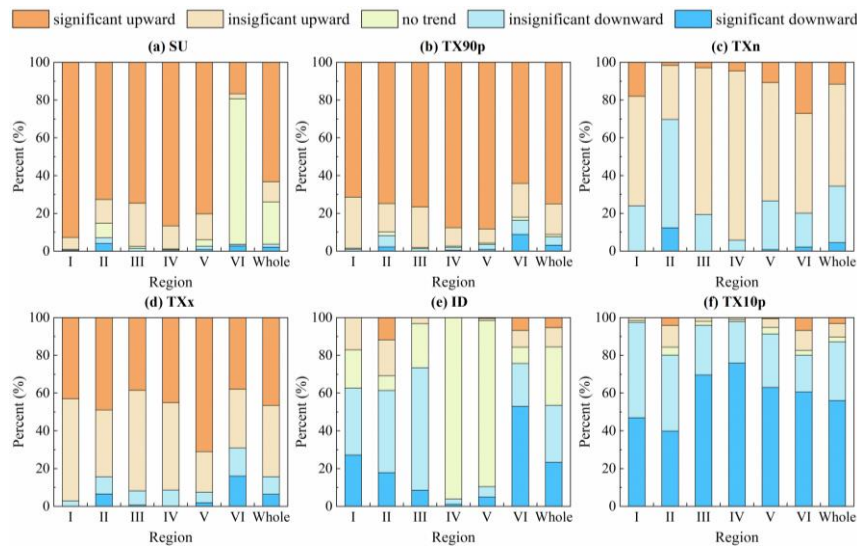
514 The spatial distribution of the extreme temperature indices trends in China during 1979-2018 is
515 shown in Fig. 4316 (a-f), while the area percentage of the increasing and decreasing trend of extreme
516 temperature indices in each region is shown in Fig. 4417 (a-f). For SU, TX90p, TXn and TXx, the
517 area with rising trend is larger than the area with declining trend. The change of SU in most regions
518 of China passed the significance test of 0.05, and the areas with significant increase accounted for
519 63.3% of the whole study area (Fig. 44a17a). The regions with no significant change in SU were
520 mainly distributed in region VI (Fig. 43a16a). There were few days in a year when T_{\max} exceeded
521 25°C in region VI, and T_{\max} in some regions was even lower than 25°C throughout the year, so the
522 change range of SU was small. The areas with a downward trend of TX90p were mainly distributed
523 in southern Xinjiang and northern Tibet (Fig. 43b16b). TX90p increased significantly in 75% of
524 regions in China ($P < 0.05$), and the area percentage of TX90p significantly increased in region V
525 was the largest among the six regions (Fig. 44b17b). The trend of TXn change in most regions of
526 China was not significant, and the significant decrease was mainly concentrated in region II and
527 region VI (Fig. 43e16c). While other regions were dominated by increasing trend of the TXn, 69.7%
528 of regions in region II showed a downward trend (Fig. 44e17c). For TXx, its upward trend was
529 slightly stronger than TXn, and the region with the highest change rate was located in western China
530 (Fig. 43d16d). The regions with significantly decreased ID were mainly distributed in region VI
531 (Fig. 43e16e). 75.7% of the regions had a declining ID, and 53% of the regions passed the
532 significance test (Fig. 44e17e). As far as TX10p is concerned, its cooling trend was much stronger
533 than that of ID, and the areas of significant decline were widely distributed through all regions of

534 China (Fig. 13f16f). The area with a significant decrease in region IV accounted for 75.9% of the
 535 region, which was the largest among the six regions (Fig. 14f17f).



536
 537 **Figure 1316.** Spatial distribution of trends in extreme temperature indices over China during 1979-2018. The

538 shaded areas indicate trends that are significant at the 0.05 level.



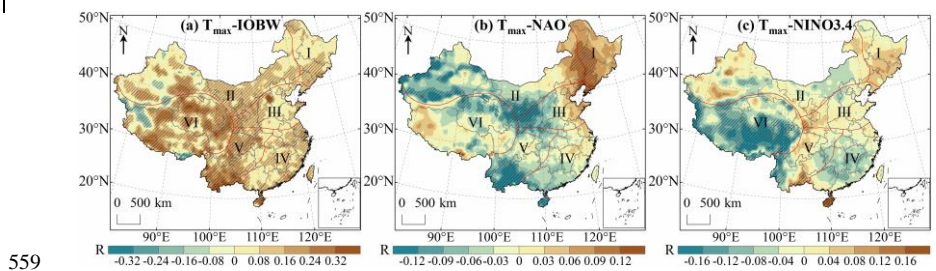
539
 540 **Figure 1417.** Area percentage of the trend of extreme temperature indices in different regions of China during

541 1979-2018

542 **6 Discussion**

543 6.1 The influence of ocean climate modalities on T_{max}

544 The correlation between T_{max} anomalies and three climate modal indices in China during 1979-2018
545 is shown in Fig. 1518 (a-c). The results show that there is a significant positive correlation between
546 T_{max} and IOBW in 54.18% of the regions in China, which indicates that the warming of the Indian
547 Ocean will contribute to the warming trend of T_{max} in these regions. T_{max} had a moderate positive
548 correlation ($0.4 < R < 0.6$, $P < 0.01$) with IOBW in southern Yunnan and eastern Hainan (Fig. 1518a).
549 T_{max} and NAO had a significant positive correlation in northeast China, but the correlation was very
550 weak ($R < 0.2$). The percentage of T_{max} anomaly value negatively correlated with NAO (16.55%)
551 was higher than that of NAO positively correlated (5.27%), mainly distributed in the west and south
552 of region II, west of region III, south of region IV and V, and northeast of region VI. This indicated
553 that the positive phase of NAO contribute to the decrease of T_{max} in these regions (Fig. 1518b).
554 T_{max} was significantly positively correlated with NINO3.4 in southern China, central Xinjiang and
555 southern Gansu, indicating that El Niño events will lead to higher temperatures in these regions. In
556 western China and the middle part of region IV, T_{max} was significantly negatively correlated with
557 NINO3.4, indicating that El Niño events will lead to cooling phenomena in these regions (Fig.
558 1518c).

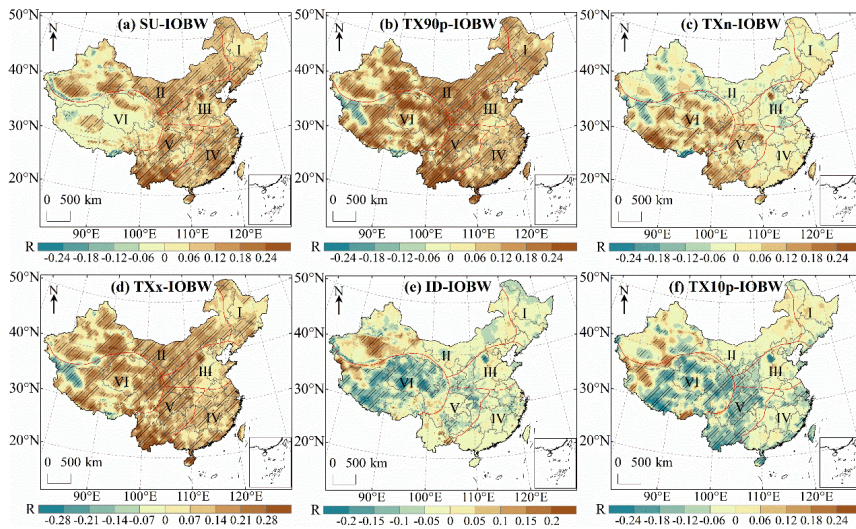


560 **Figure 1518.** Correlation analysis between T_{max} and IOBW (a), NAO (b) and NINO3.4 (c) in China during 1979-
561 2018. The shaded areas indicate correlations that are significant at the 0.05 level.

562 6.2 The influence of ocean climate mode on extreme temperature indices

563 Fig. 1619 (a-f) indicates the spatial distribution of the correlation between extreme temperature
564 indices anomalies and IOBW in China during 1979-2018. It can be seen that SU, TX90p, TXn and
565 TXx over most of China are positively correlated with the IOBW. The region with significant
566 positive correlation between the SU and IOBW accounted for 42.67% of the whole study area, which
567 indicated that a warming Indian Ocean would lead to the number of days over 25°C in these regions
568 to increase. Significant negative correlations were found in northwest and southeast Tibet and the
569 mountainous regions of southern Xinjiang (Fig. 1619a). The area with the largest correlation
570 coefficient is in the northeast of Hainan ($R=0.48$). The significant negative correlation between
571 TX90p and IOBW was mainly distributed in region VI, but the negative correlation was not strong
572 ($|R| < 0.4$) (Fig. 1619b). The correlation coefficient between TXn and IOBW ranged from -0.34 to
573 0.34, and the regions with significant positive correlation accounted for 16.65% of the whole study
574 area. TXn and IOBW were significantly negatively correlated mainly in western China (Fig.
575 1619c). Compared with TXn, the regions with significant correlation between TXx and IOBW
576 were more widely distributed in China, among which the correlation coefficients in southern
577 Yunnan and eastern Hainan were moderately positive ($0.4 < R < 0.6$) (Fig. 1619d). ID and TX10p
578 were negatively correlated with IOBW in most of China. The regions with significant negative
579 correlation between ID and IOBW were mainly distributed in region VI, and the regions with
580 significant positive correlation were mainly distributed in the west of region II (Fig. 1619e). TX10p

581 has a significant negative correlation with IOBW in more areas than ID, and the significant positive
 582 correlation was mainly located in western China (Fig. 16f19f).

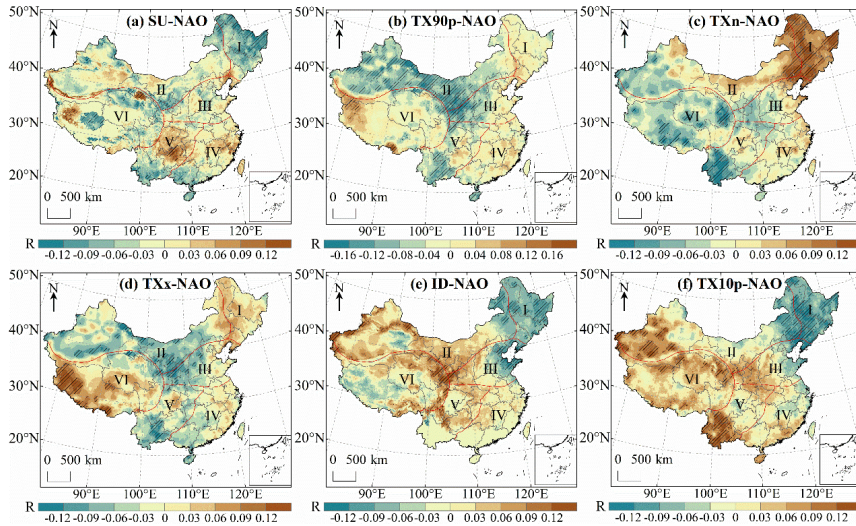


583
 584 **Figure 16f19.** Correlation analysis between extreme temperature indices and IOBW in China during 1979-2018.

585 The shaded areas indicate correlations that are significant at the 0.05 level.

586 The influence of NAO on the extreme temperature indices is shown in Fig. 17a20 (a-f). SU,
 587 TX90p, TXx and TXn were negatively correlated with the NAO more than they were positively
 588 correlated with NAO, indicating that the positive phase of NAO would lead to the decline of SU,
 589 TX90p, TXx and TXn over most of China. SU and NAO had a significant positive correlation in
 590 southern Xinjiang, western Tibet, northern Qinghai and northern Guizhou, but the correlation was
 591 very weak ($R < 0.2$). There was no significant correlation between SU and NAO in southern Qinghai,
 592 which was consistent with previous observations (Ding et al., 2018). The region with the strongest
 593 negative correlation between SU and NAO was located in Tibet ($R = -0.18$) (Fig. 17a20a). TX90p
 594 had a weak negative correlation with NAO in eastern Xinjiang ($R = -0.22$, $P < 0.01$). TX90p was
 595 significantly positively correlated with NAO in the west and south of region VI, but the correlation

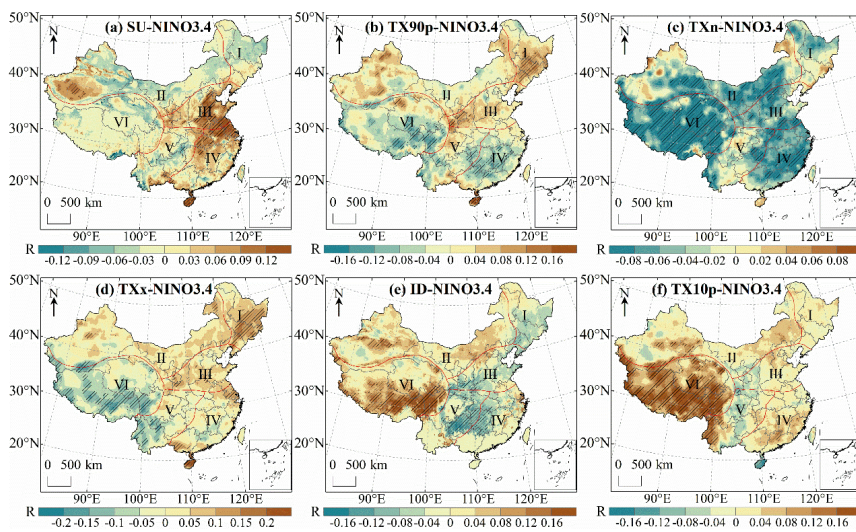
596 was extremely weak (Fig. [17b20b](#)). Shi et al. (2019) indicated that more regions had a significant
597 positive correlation between TXn and NAO in China than had a significant negative correlation,
598 which was consistent with our results. The areas of TXn had a significant positive correlation with
599 NAO were mainly distributed in northeast China, while the regions with significant negative
600 correlation were mainly located in central Tibet, eastern Qinghai and Yunnan (Fig. [17e20c](#)). The
601 correlation coefficient between TXx and NAO varied from -0.16 to 0.21. The regions with
602 significant positive correlation between TXx and NAO were mainly located in Tibet, and the region
603 with the strongest correlation was located in southern Tibet (Fig. [17d20d](#)). The areas of ID was
604 significantly positively correlated with NAO accounted for 5.86% of the whole study area, and the
605 strongest correlation was found in western Xinjiang ($R=0.23$). The regions with significant negative
606 correlation between ID and NAO were mainly distributed in eastern and northeastern China (Fig.
607 [17e20e](#)). Sun et al. (2016) found a very weak positive correlation between TX10p and NAO in the
608 Loess Plateau, which was consistent with our results. The regions with a significant negative
609 correlation were mainly concentrated in northeastern China (Fig. [17f20f](#)).



610
 611 **Figure 18.20.** Correlation analysis between extreme temperature indices and NAO in China during 1979-2018. The
 612 shaded areas indicate correlations that are significant at the 0.05 level.

613 Fig. 18.21 (a-f) shows the correlation between NINO3.4 and extreme temperature indices. The
 614 regions with significant positive correlation between SU and NINO3.4 were mainly distributed in
 615 eastern China, indicating that the events of El Niño would lead to an upward trend of SU in these
 616 regions. There were few regions with significant negative correlation between SU and NINO3.4,
 617 only accounting for 1.15% of the entire research area, mainly distributed in southeast Tibet and
 618 southwest Yunnan (Fig. 18.21a). The correlation coefficient between TX90p and NINO3.4 was -
 619 0.19-0.26. The areas of TX90p had a significant negative correlation with NINO3.4 were mainly
 620 distributed in region IV and VI (Fig. 18.21b). There was a significant negative correlation between
 621 TXn and NINO3.4 in 24.59% of regions, and the region with the strongest negative correlation was
 622 located in Tibet ($R=-0.25$). TXn was positively correlated with NINO3.4 in only 10.46% of regions
 623 in China, and the region with the largest correlation coefficient was northwest Xinjiang ($R=0.11$)
 624 (Fig. 18.21c). There was a weak positive correlation between TXx and NINO3.4 in southern

625 Guangdong and northern Hainan ($0.2 < R < 0.4$). The regions of TXx was significantly negatively
 626 correlated with NINO3.4 were mainly distributed in the south of region V and region VI (Fig.
 627 [18f21d](#)). The significant negative correlation between ID and NINO3.4 was mainly concentrated in
 628 southern China. The areas with significant positive correlation were mainly distributed in the
 629 western region II and southern region VI, and the region with the strongest correlation was located
 630 in the western Sichuan ($R=0.31$) (Fig. [18e21e](#)). TX10p in most regions of regional VI was
 631 significantly affected by NINO3.4, and the significant positive correlation area accounted for 69.31%
 632 of the whole region VI. TX10p was significantly negatively correlated with NINO3.4 in only 0.65%
 633 of regions in China, mainly distributed in Hainan and southern Gansu (Fig. [18f21f](#)).



634
 635 **Figure 1821.** Correlation analysis between extreme temperature indices and NINO3.4 in China during 1979-2018.

636 The shaded areas indicate correlations that are significant at the 0.05 level.

637 7 Conclusions

638 The global temperature continues to rise and extreme weather events continue to increase (IPCC,
 639 2021). It is great significance to study regional high temperature changes. In order to obtain the key

640 parameters of high temperature spatial-temporal variation analysis, this study proposed a daily T_{\max}
641 estimation frame based on the near-surface T_a grid data and T_a diurnal variation model to build a
642 T_{\max} dataset in China from 1979 to 2018. Validation of T_{\max} estimation data in six natural regions
643 indicated that the RMSE of each region was between 2.38-2.94 °C, the MAE was between 1.88-
644 2.45 °C, and R^2 was between 0.95-0.99. After using the regression model to calibrate the dataset, the
645 accuracy of the estimated T_{\max} has been significantly improved. The RMSE of the T_{\max} after
646 calibration reduced to 1.14-1.81 °C, and the MAE reduced to 0.84-1.38 °C, and the R^2 increased to
647 0.97-0.99.

648 This dataset was used to study the spatial-temporal variation characteristics of T_{\max} and the
649 corresponding influencing factors in China, and to discuss the correlation between T_{\max} , extreme
650 temperature indices and ocean climate modal indices. T_{\max} in all regions of China exhibited an
651 upward trend from 1979 to 2018, with the largest rise in region V and the smallest rise in region I.
652 In spring, T_{\max} in China increased significantly in most regions, and the region III is with the fastest
653 rising speed. In winter, T_{\max} in China had the least significant rise, and the region II was with the
654 slowest rise rate. SU, TX90p and TXx in all regions showed an upward trend. Except for region II,
655 TXn in other regions also exhibited an upward trend, while ID and TX10p in all regions showed a
656 downward trend. All extreme temperature indices had abrupt changes during 1979-2018, and most
657 of the abrupt changes occurred in El Niño or La Niña years. The region with the largest increase of
658 SU, TX90p and TXx and the region with the largest decrease of TX10p were located in the western
659 Yunnan. The correlation analysis between T_{\max} and extreme temperature indices and ocean climate
660 modal indices indicated that the increase of the IOBW usually coincides with the increase of T_{\max} ,
661 SU, TX90p, TXn and TXx and the decrease of ID and TX10p. NAO had the opposite relationships.

662 In most regions of China, T_{\max} , SU, TX90p and TXn were negatively correlated with NINO.3.4,
663 while TXx, ID and TX10p were positively correlated with NINO.3.4.

664 The T_{\max} dataset we produced can not only be used as the input parameters of climate change
665 models, crop growth models and carbon emission models, but also can be used to evaluate the risk
666 of high temperature disasters, which has high practical value. Currently, due to the limitation of the
667 temporal and spatial scope of the basic data, we have only produced the dataset of China. If global
668 station data and temperature data can be obtained in the future, we can continue to produce T_{\max}
669 dataset on a global scale. The analysis of regional high temperature temporal and spatial changes
670 shows that the temperature changes in different regions of China are inconsistent, and the
671 mechanism that affects the temperature rise is different in different regions, and some regions are
672 highly correlated with ocean temperature changes. China is located in the eastern Eurasian continent
673 and the western Pacific Ocean. With the influence of the unique topography of the Qinghai-Tibet
674 Plateau, China's climate system is very complex. The temperature change in China is affected by a
675 combination of factors, and the ocean is only one of the factors affecting the temperature change in
676 China. Our study found that the influence of the ocean on China's temperature change is not
677 particularly strong, and we can continue to study the driving factors that have a strong impact on
678 China's climate change in the future. In order to strengthen environmental protection and control
679 temperature rise, and formulate reasonable carbon emission reduction measures, we need further
680 research in the future.

681

682 *Code and Data availability.* CMFD is available from the National Qinghai-Tibet Plateau Science
683 Data Center (<https://data.tpdc.ac.cn/>). ERA5 data can be obtained from Copernicus Climate Data

684 Store (<https://cds.climate.copernicus.eu/>). Meteorological station data is available by CMA National
685 Meteorological Information Center (<http://data.cma.cn/>). IOBW index can be accessed at the
686 National Climate Center of CMA (<http://cmdp.ncc-cma.net/cn/index.htm>), and NAO index and
687 NINO3.4 index are from the National Oceanic and Atmospheric Administration of the United States
688 (<https://psl.noaa.gov/data/climateindices/list/>). The daily highest air temperature dataset and code
689 can be downloaded at <https://doi.org/10.5281/zenodo.6322881> (Wang et al., 2021).

690

691 *Author contributions.* KM and PW proposed the goals and aims of the research. KM provided
692 supervision and scientific guidance for the research. PW and SF built the dataset production model.
693 PW wrote the paper. KM, FM, ZQ, and SMB revised the final manuscript.

694

695 *Competing interests.* The authors declare no conflicts of interest.

696

697 *Acknowledgements.* The authors thank the China Meteorological Administration for providing
698 IOBW index and the ground measurements data, the Institute of Tibetan Plateau Research, Chinese
699 Academy of Sciences for providing CMFD dataset, and the NASA Earth Observing System Data
700 and Information System for providing the DEM data. We also thank the National Oceanic and
701 Atmospheric Administration of the United States for providing the ocean climate modal indices and
702 the ECMWF for providing the climate reanalysis data.

703

704 *Financial support.* This work is supported by the Framework Project of APSCO Member States
705 (Global and key regional drought forecasting and monitoring) and the National Key Research and

706 Development Program of China (2019YFE0127600), Ningxia Science and Technology Department

707 Flexible introduction talent project (No.2021RXTDLX14).

708

709 **References**

- 710 Abdullah, A. M., Ismail, M., Yuen, F. S., Abdullah, S., and Elhadi, R. E.: The Relationship between
711 Daily Maximum Temperature and Daily Maximum Ground Level Ozone Concentration, Polish
712 Journal of Environmental Studies, 26, 517-523, <https://doi.org/10.15244/pjoes/65366>, 2017.
- 713 Basu, R.: High ambient temperature and mortality: a review of epidemiologic studies from 2001 to 2008,
714 Environmental health, 8, 40, <https://doi.org/10.1186/1476-069X-8-40>, 2009.
- 715 Benali, A., Carvalho, A. C., Nunes, J. P., Carvalhais, N., and Santos, A.: Estimating air surface
716 temperature in Portugal using MODIS LST data, Remote Sensing of Environment, 124, 108-121,
717 <https://doi.org/10.1016/j.rse.2012.04.024>, 2012.
- 718 Ding, Z. Y., Wang, Y. Y., and Lu, R. J.: An analysis of changes in temperature extremes in the Three
719 River Headwaters region of the Tibetan Plateau during 1961-2016, Atmospheric Research, 209, 103-
720 114, <https://doi.org/10.1016/j.atmosres.2018.04.003>, 2018.
- 721 Du, Q. Q., Zhang, M. J., Wang, S. J., Che, C. W., Ma, R., and Ma, Z. Z.: Changes in air temperature over
722 China in response to the recent global warming hiatus, Journal of Geographical Sciences, 29, 496-516,
723 <https://doi.org/10.1007/s11442-019-1612-3>, 2019.
- 724 Ephrath, J. E., Goudriaan, J., and Marani, A.: Modelling diurnal patterns of air temperature, radiation
725 wind speed and relative humidity by equations from daily characteristics, Agricultural Systems, 51,
726 377-393, [https://doi.org/10.1016/0308-521X\(95\)00068-G](https://doi.org/10.1016/0308-521X(95)00068-G), 1996.
- 727 Evrendilek, F., Karakaya, N., Gungor, K., and Aslan, G.: Satellite-based and mesoscale regression
728 modeling of monthly air and soil temperatures over complex terrain in Turkey, Expert Systems with
729 Applications, 39, 2059-2066, <https://doi.org/10.1016/j.eswa.2011.08.023>, 2012.
- 730 Fabiola, F. P. and Mario, L. S.: Simple air temperature estimation method from MODIS satellite images
731 on a regional scale, Chilean Journal of Agricultural Research, 70, 436-445,
732 <https://doi.org/10.4067/S0718-58392010000300011>, 2010.
- 733 Gasparrini, A. and Armstrong, B.: The impact of heat waves on mortality, Epidemiology, 22, 68-73,
734 <https://doi.org/10.1097/EDE.0b013e3181fdcd99>, 2011.
- 735 Gu, H. H., Yu, Z. B., Peltier, W. R., and Wang, X. Y.: Sensitivity studies and comprehensive evaluation
736 of RegCM4. 6.1 high-resolution climate simulations over the Tibetan Plateau, Climate Dynamics, 54,
737 3781-3801, <https://doi.org/10.1007/s00382-020-05205-6>, 2020.
- 738 Guan, Y. H., Zhang, X. C., Zheng, F. L., and Wang, B.: Trends and variability of daily temperature
739 extremes during 1960–2012 in the Yangtze River Basin, China, Global and Planetary Change, 124,
740 79-94, <https://doi.org/10.1016/j.gloplacha.2014.11.008>, 2015.
- 741 He, J., Yang, K., Tang, W. J., Lu, H., Qin, J., Chen, Y. Y., and Li, X.: The first high-resolution
742 meteorological forcing dataset for land process studies over China, Scientific Data 7, 1-11,
743 <https://doi.org/10.1038/s41597-020-0369-y>, 2020.
- 744 Hersbach, H., Bell, B., Berrisford, P., Hirahara, S., Horányi, A., Muñoz - Sabater, J., Nicolas, J., Peubey,
745 C., Radu, R., Schepers, D., Simmon, A., Soci, C., Abdalla, S., Abellan, X., Balsamo, G., Bechtold, P.,

746 Biavati, G., Bidlot, J., Bonavita, M., De Chiara, G., Dahlgren, P., Dee, D., Diamantakis, M., Dragani,
747 R., Flemming, J., Forbes, R., Fuentes, M., Geer, A., Haimberger, L., Healy, S., Hogan, R. J., Hólm,
748 E., Janisková, M., Keeley, S., Laloyaux, P., Lopez, P., Lupu, C., Radnoti, G., de Rosnay, P., Rozum,
749 I., Vamborg, F., Villaume, S., and Thépaut, J.-N.: The ERA5 global reanalysis, *Quarterly Journal of*
750 *the Royal Meteorological Society*, 146, 1999-2049, <https://doi.org/10.1002/qj.3803>, 2020.

751 Hoffmann, L., Günther, G., Li, D., Stein, O., Wu, X., Griessbach, S., Heng, Y., Konopka, P., Müller, R.,
752 Vogel, B., and Wright, J. S.: From ERA-Interim to ERA5: the considerable impact of ECMWF's next-
753 generation reanalysis on Lagrangian transport simulations, *Atmospheric Chemistry and Physics*, 19,
754 3097-3124, <https://doi.org/10.5194/acp-19-3097-2019>, 2019.

755 Hong, Y. and Ying, S.: Characteristics of extreme temperature and precipitation in China in 2017 based
756 on ETCCDI indices, *Advances in Climate Change Research*, 9, 218-226,
757 <https://doi.org/10.1016/j.accre.2019.01.001>, 2018.

758 IPCC: *Weather and Climate Extreme Events in a Changing Climate*, Cambridge University Press,
759 Cambridge, <https://doi.org/10.1017/9781009157896.013>, 2021.

760 Johnson, M. E. and Fitzpatrick, E. A.: A comparison of two methods of estimating a mean diurnal
761 temperature curve during the daylight hours, *Archiv für Meteorologie, Geophysik und*
762 *Bioklimatologie, Serie B*, 25, 251-263, <https://doi.org/10.1007/BF02243056>, 1977.

763 Khan, N., Shahid, S., Ismail, T. B., and Wang, X. J.: Spatial distribution of unidirectional trends in
764 temperature and temperature extremes in Pakistan, *Theoretical and Applied Climatology*, 136, 899-
765 913, <https://doi.org/10.1007/s00704-018-2520-7>, 2018.

766 Kleinert, F., Leufen, L. H., and Schultz, M. G.: IntelliO3-ts v1. 0: a neural network approach to predict
767 near-surface ozone concentrations in Germany, *Geoscientific Model Development*, 14, 1-25,
768 <https://doi.org/10.5194/gmd-14-1-2021>, 2021.

769 Li, L. C., Yao, N., Li, Y., Liu, D. L., Wang, B., and Ayantobo, O. O.: Future projections of extreme
770 temperature events in different sub-regions of China, *Atmospheric Research*, 217, 150-164,
771 <https://doi.org/10.1016/j.atmosres.2018.10.019>, 2019a.

772 Li, Q. X., Yang, S., Xu, W. H., Wang, X. L., Jones, P., Parker, D., Zhou, L. M., Feng, Y., and Gao, Y.:
773 China experiencing the recent warming hiatus, *Geophysical Research Letters*, 42, 889-898,
774 <https://doi.org/10.1002/2014GL062773>, 2015.

775 Li, Y. L., Han, W. Q., Zhang, L., and Wang, F.: Decadal SST variability in the southeast Indian Ocean
776 and its impact on regional climate, *Journal of Climate*, 32, 6299-6318, [https://doi.org/10.1175/JCLI-](https://doi.org/10.1175/JCLI-D-19-0180.1)
777 [D-19-0180.1](https://doi.org/10.1175/JCLI-D-19-0180.1), 2019b.

778 Lin, S. P., Moore, N. J., Messina, J. P., DeVisser, M. H., and Wu, J. P.: Evaluation of estimating daily
779 maximum and minimum air temperature with MODIS data in east Africa, *International Journal of*
780 *Applied Earth Observation and Geoinformation*, 18, 128-140,
781 <https://doi.org/10.1016/j.jag.2012.01.004>, 2012.

782 Luan, J. K., Zhang, Y. Q., Tian, J., Meresa, H. K., and Liu, D. F.: Coal mining impacts on catchment
783 runoff, *Journal of Hydrology*, 589, 125101, <https://doi.org/10.1016/j.jhydrol.2020.125101>, 2020.

784 McGree, S., Herold, N., Alexander, L., Schreider, S., Kuleshov, Y., Ene, E., Finaulahi, S., Inape, K.,
785 Mackenzie, B., Malala, H., Ngari, A., Prakash, B., and Tahani, L.: Recent changes in mean and
786 extreme temperature and precipitation in the Western Pacific Islands, *Journal of Climate*, 32, 4919-
787 4941, <https://doi.org/10.1175/JCLI-D-18-0748.1> 2019.

788 Ninyerola, M., Pons, X., and Roure, J. M.: A methodological approach of climatological modelling of
789 air temperature and precipitation through GIS techniques, *International Journal of Climatology*, 20,

790 1823-1841, [https://doi.org/10.1002/1097-0088\(20001130\)20:14<1823::AID-JOC566>3.0.CO;2-B](https://doi.org/10.1002/1097-0088(20001130)20:14<1823::AID-JOC566>3.0.CO;2-B),
791 2000.

792 Parton, W. J. and Logan, J. A.: A model for diurnal variation in soil and air temperature, *Agricultural*
793 *Meteorology*, 23, 205-216, [https://doi.org/10.1016/0002-1571\(81\)90105-9](https://doi.org/10.1016/0002-1571(81)90105-9), 1981.

794 Poudel, A., Cuo, L., Ding, J., and Gyawali, A. R.: Spatio - temporal variability of the annual and monthly
795 extreme temperature indices in Nepal, *International Journal of Climatology*, 40, 4956-4977,
796 <https://doi.org/10.1002/joc.6499>, 2020.

797 Ruml, M., Gregorić, E., Vujadinović, M., Radovanović, S., Matović, G., Vuković, A., Počuča, V., and
798 Stojičić, D.: Observed changes of temperature extremes in Serbia over the period 1961 – 2010,
799 *Atmospheric Research*, 183, 26-41, <https://doi.org/10.1016/j.atmosres.2016.08.013>, 2017.

800 Salman, S. A., Shahid, S., Ismail, T., Chung, E.-S., and Al-Abadi, A. M.: Long-term trends in daily
801 temperature extremes in Iraq, *Atmospheric Research*, 198, 97-107,
802 <https://doi.org/10.1016/j.atmosres.2017.08.011>, 2017.

803 Sathaye, J. A., Dale, L. L., Larsen, P. H., Fitts, G. A., Koy, K., Lewis, S. M., and de Lucena, A. F. P.:
804 Estimating impacts of warming temperatures on California's electricity system, *Global Environmental*
805 *Change*, 23, 499-511, <https://doi.org/10.1016/j.gloenvcha.2012.12.005>, 2013.

806 Seenu, P. Z. and Jayakumar, K. V.: Comparative study of innovative trend analysis technique with Mann-
807 Kendall tests for extreme rainfall, *Arabian Journal of Geosciences*, 14, 1-15,
808 <https://doi.org/10.1007/s12517-021-06906-w>, 2021.

809 Sehra, S. T., Salciccioli, J. D., Wiebe, D. J., Fundin, S., and Baker, J. F.: Maximum daily temperature,
810 precipitation, ultraviolet light, and rates of transmission of severe acute respiratory syndrome
811 coronavirus 2 in the United States, *Clinical Infectious Diseases*, 71, 2482-2487,
812 <https://doi.org/10.1093/cid/ciaa681>, 2020.

813 Sen, P. K.: Estimates of the regression coefficient based on Kendall's tau, *Journal of the American*
814 *Statistical Association*, 63, 1379-1389, <https://doi.org/10.2307/2285891> 1968.

815 Shen, S. H. and Leptoukh, G. G.: Estimation of surface air temperature over central and eastern Eurasia
816 from MODIS land surface temperature, *Environmental Research Letters*, 6, 045206,
817 <https://doi.org/10.1088/1748-9326/6/4/045206> 2011.

818 Shi, J., Cui, L. L., Wang, J. B., Du, H. Q., and Wen, K. M.: Changes in the temperature and precipitation
819 extremes in China during 1961–2015, *Quaternary International*, 527, 64-78,
820 <https://doi.org/10.1016/j.quaint.2018.08.008>, 2019.

821 Sun, W. Y., Mu, X. M., Song, X. Y., Wu, D., Cheng, A. F., and Qiu, B.: Changes in extreme temperature
822 and precipitation events in the Loess Plateau (China) during 1960–2013 under global warming,
823 *Atmospheric Research*, 168, 33-48, <http://dx.doi.org/10.1016/j.atmosres.2015.09.001>, 2016.

824 Sun, Y. J., Wang, J. F., Zhang, R. H., Gillies, R. R., Xue, Y., and Bo, Y. C.: Air temperature retrieval
825 from remote sensing data based on thermodynamics, *Theoretical and Applied Climatology*, 80, 37-48,
826 <https://doi.org/10.1007/s00704-004-0079-y>, 2005.

827 Tan, M. L., Samat, N., Chan, N. W., Lee, A. J., and Li, C.: Analysis of Precipitation and Temperature
828 Extremes over the Muda River Basin, Malaysia, *Water*, 11, 1-16, <https://doi.org/10.3390/w11020283>,
829 2019.

830 Tong, S. Q., Li, X. Q., Zhang, J. Q., Bao, Y. H., Bao, Y. B., Na, L., and Si, A. L.: Spatial and temporal
831 variability in extreme temperature and precipitation events in Inner Mongolia (China) during 1960–
832 2017, *Science of the Total Environment*, 649, 75-89, <https://doi.org/10.1016/j.scitotenv.2018.08.262>,
833 2019.

834 Urraca, R., Huld, T., Gracia-Amillo, A., Martinez-de-Pison, F. J., Kaspar, F., and Sanz-Garcia, A.:
835 Evaluation of global horizontal irradiance estimates from ERA5 and COSMO-REA6 reanalyses using
836 ground and satellite-based data, *Solar Energy*, 164, 339-354,
837 <https://doi.org/10.1016/j.solener.2018.02.059>, 2018.

838 Wang, X. X., Jiang, D. B., and Lang, X. M.: Extreme temperature and precipitation changes associated
839 with four degree of global warming above pre - industrial levels, *International Journal of Climatology*,
840 39, 1822-1838, <https://doi.org/10.1002/joc.5918>, 2019.

841 Wang, Y., Peng, D. L., Shen, M. G., Xu, X. Y., Yang, X. H., Huang, W. J., Yu, L., Liu, L. Y., Li, C. J.,
842 and Li, X. W.: Contrasting Effects of Temperature and Precipitation on Vegetation Greenness along
843 Elevation Gradients of the Tibetan Plateau, *Remote Sensing*, 12, 2751,
844 <https://doi.org/10.3390/rs12172751>, 2020.

845 Wloczyk, C., Borg, E., Richter, R., and Miegel, K.: Estimation of instantaneous air temperature above
846 vegetation and soil surfaces from Landsat 7 ETM+ data in northern Germany, *International Journal of*
847 *Remote Sensing*, 32, 9119-9136, <https://doi.org/10.1080/01431161.2010.550332>, 2011.

848 Wu, R. G., Yang, S., Liu, S., Sun, L., Lian, Y., and Gao, Z. T.: Northeast China summer temperature and
849 north Atlantic SST, *Journal of Geophysical Research*, 116, <https://doi.org/10.1029/2011JD015779>,
850 2011.

851 Yang, Z. Y., Shen, M. G., Jia, S. G., Guo, L., Yang, W., Wang, C., Chen, X. H., and Chen, J.: Asymmetric
852 responses of the end of growing season to daily maximum and minimum temperatures on the Tibetan
853 Plateau, *Journal of Geophysical Research*, 122, 278-287, <https://doi.org/10.1002/2017JD027318>,
854 2017.

855 Yoo, C., Im, J., Park, S., and Quackenbush, L. J.: Estimation of daily maximum and minimum air
856 temperatures in urban landscapes using MODIS time series satellite data, *ISPRS Journal of*
857 *Photogrammetry and Remote Sensing*, 137, 149-162, <https://doi.org/10.1016/j.isprsjprs.2018.01.018>,
858 2018.

859 You, Q. L., Kang, S. C., Aguilar, E., Pepin, N., Flügel, W.-A., Yan, Y. P., Xu, Y. W., Zhang, Y. J., and
860 Huang, J.: Changes in daily climate extremes in China and their connection to the large scale
861 atmospheric circulation during 1961–2003, *Climate Dynamics*, 36, 2399-2417,
862 <https://doi.org/10.1007/s00382-009-0735-0>, 2011.

863 Zhai, P. M., Yu, R., Guo, Y. J., Li, Q. X., Ren, X. J., Wang, Y. Q., Xu, W. H., Liu, Y. J., and Ding, Y.
864 H.: The strong El Niño in 2015/2016 and its dominant impacts on global and China's climate, *Acta*
865 *Meteorologica Sinica*, 74, 309-321. (In Chinese), <https://doi.org/10.11676/qxxb2016.049>, 2016.

866 Zhang, H., Da, Y. B., Zhang, X., and Fan, J. L.: The impacts of climate change on coal-fired power plants:
867 evidence from China, *Energy & Environmental Science*, 14, 4890-4902,
868 <https://doi.org/10.1039/D1EE01475G>, 2021.

869 Zhang, M., Du, S. Q., Wu, Y. J., Wen, J. H., Wang, C. X., Xu, M., and Wu, S. Y.: Spatiotemporal changes
870 in frequency and intensity of high-temperature events in China during 1961-2014, *Journal of*
871 *Geographical Sciences*, 27, 1027-1043, <https://doi.org/10.1007/s11442-017-1419-z>, 2017.

872 Zhang, P. F., Ren, G. Y., Xu, Y., Wang, X. L. L., Qin, Y., Sun, X. B., and Ren, Y. Y.: Observed changes
873 in extreme temperature over the global land based on a newly developed station daily dataset, *Journal*
874 *of Climate*, 32, 8489-8509, <https://doi.org/10.1175/JCLI-D-18-0733.1> 2019.

875 Zhao, B., Mao, K. B., Cai, Y. L., Shi, J. C., Li, Z. L., Qin, Z. H., Meng, X. J., Shen, X. Y., and Guo, Z.
876 H.: A combined Terra and Aqua MODIS land surface temperature and meteorological station data

877 product for China from 2003 to 2017, *Earth System Science Data*, 12, 2555-2577,
878 <https://doi.org/10.5194/essd-12-2555-2020>, 2020.

879 Zheng, X., Zhu, J. J., and Yan, Q. L.: Monthly air temperatures over Northern China estimated by
880 integrating MODIS data with GIS techniques, *Journal of Applied Meteorology and Climatology*, 52,
881 1987-2000, <https://doi.org/10.1175/JAMC-D-12-0264.1> 2013.

882 Zhong, K. Y., Zheng, F. L., Wu, H. Y., Qin, C., and Xu, X. M.: Dynamic changes in temperature extremes
883 and their association with atmospheric circulation patterns in the Songhua River Basin, China,
884 *Atmospheric Research*, 190, 77-88, <https://doi.org/10.1016/j.atmosres.2017.02.012>, 2017.

885 Zhou, B. T., Xu, Y., Wu, J., Dong, S. Y., and Shi, Y.: Changes in temperature and precipitation extreme
886 indices over China: Analysis of a high - resolution grid dataset, *International Journal of Climatology*,
887 36, 1051-1066, <https://doi.org/10.1002/joc.4400>, 2016.

888 Zhu, S. Y., Zhou, C. X., Zhang, G. X., Zhang, H. L., and Hua, J. W.: Preliminary verification of
889 instantaneous air temperature estimation for clear sky conditions based on SEBAL, *Meteorology and*
890 *Atmospheric Physics*, 129, 71-81, <https://doi.org/10.1007/s00703-016-0451-3>, 2017.

891 Zhu, W. B., Lü, A. F., and Jia, S. F.: Estimation of daily maximum and minimum air temperature using
892 MODIS land surface temperature products, *Remote Sensing of Environment*, 130, 62-73,
893 <http://dx.doi.org/10.1016/j.rse.2012.10.034>, 2013.

894